Contents lists available at ScienceDirect

Acta Materialia

journal homepage: www.elsevier.com/locate/actamat

Full length article

Phase-field investigation on the microstructural evolution of eutectic transformation and four-phase reaction in Mo-Si-Ti system

Yuhan Cai [a], Fei Wang [a,c,*], Andreas Czerny [b], Hans Jürgen Seifert [b], Britta Nestler [a,c,d]

[a] Institute for Applied Materials - Microstructure Modeling and Simulation (IAM-MMS), Karlsruhe Institute of Technology (KIT), Straße am Forum 7, 76131 Karlsruhe, Germany
[b] Institute for Applied Materials - Applied Materials Physics (IAM-AWP), Karlsruhe Institute of Technology (KIT), Hermann-von-Helmholtz-Platz 1, 76344 Eggenstein-Leopoldshafen, Germany
[c] Institute of Nanotechnology (INT), Karlsruhe Institute of Technology (KIT), Hermann-von-Helmholtz-Platz 1, 76344 Eggenstein-Leopoldshafen, Germany
[d] Institute of Digital Materials Science, Karlsruhe University of Applied Sciences, Moltkestrasse 30, 76133 Karlsruhe, Germany

ARTICLE INFO

ABSTRACT

By using phase-field method, we investigate the morphological evolution of three-phase eutectic transition and four-phase reaction in Mo-Si-Ti system through 2-D and 3-D simulations. For the eutectic transition, we focus on the two-phase growth of lamellar pair from an isothermally undercooled melt: $L \rightarrow Ti(Mo)_5Si_3 + \beta(Mo,Si,Ti)$, and obtain a microstructure selection map for (m_i) stable, (m_{ii}) unstable, and (m_{iii}) oscillatory growth (metastable mode), in terms of the Mo-composition and lamellar spacings. The underlying reason for these three different morphologies is clarified by analyzing the growth rate of the solidification front. In addition, we scrutinize the influence of interfacial energy on the solidification morphology and observe three different types of growth mode: (g_i) curving, (g_{ii}) stable, and (g_{iii}) unstable growth. For the four-phase reaction, $L + Mo(Ti)_3Si \rightarrow Ti(Mo)_5Si_3 + \beta(Mo,Si,Ti)$, we observe the remelting of $Mo(Ti)_3Si$ phase and the formation of a lamellar pair consisting of $Ti(Mo)_5Si_3$ and $\beta(Mo,Si,Ti)$ on the surface of the $Mo(Ti)_3Si$ phase after an interface of the lamellae pair phases is formed. A certain orientation angle with respect to the solidification direction is obtained for the lamellar pair growth during the four-phase reaction. In both eutectic phase transformation and four phase reaction, a comparison between the 2D and 3D simulations reveals the influence of the third dimension on the development of the lamellar pair.

1. Introduction

In past decades, Mo-Si-based alloys have drawn increasing attention due to its potential as alternative materials to Ni-based superalloys for high temperature structural applications [1,2]. Besides good creep resistance and high melting point, Mo-Si-based alloy exhibits a significant reduction in density, which is a considerable advantage compared to Ni-based alloy [3]. However, inadequate oxidation resistance, especially at intermediate temperature below 1000 °C, is still a challenge for its industrial utilization. To address this issue, Schliephake et al. developed a two-phase eutectic Mo-Si-Ti alloy that shows great potential [4] for industrial application. On the basis of the work [4], Obert et al. found a novel eutectic-eutectoid two-phase Mo-Si-Ti alloy that shows both outstanding oxidation resistance and sufficient creep resistance [5]. In these alloys, the $Ti(Mo)_5Si_3$ and $\beta(Mo,Si,Ti)$ lamellae, formed during the solidification process, play a vital role in the oxidation as well as in the creep behavior. Therefore, it is meaningful to

systematically study the morphological evolution of lamellae in Mo-Si-Ti alloy. According to the previous work by Yang et al. [6], lamellae microstructures can be produced either by eutectic transformation ($L \rightarrow Ti(Mo)_5Si_3 + \beta(Mo,Si,Ti)$) or by a quasi-peritectic four-phase reaction ($L + Mo(Ti)_3Si \rightarrow Ti(Mo)_5Si_3 + \beta(Mo,Si,Ti)$). Hence, in the present study, we focus on this lamellae growth produced by an eutectic transformation as well as by a four-phase reaction.

It is a daunting task to investigate the phase transformation statistically and theoretically by carefully controlled experiments. Therefore, it is of great significance and feasibility to shed light on the growth of the $Ti(Mo)_5Si_3$ and $\beta(Mo,Si,Ti)$ lamellae, by using computational materials simulations. The phase-field method has been proven to be a powerful modeling technique to simulate the growth of intermetallic compounds in many alloy systems, e.g. Sn-Cu [7,8], Al-Au [9], Fe-Cr-Ni [10] and Al-Cu-Mg [11]. Among these mentioned works, more attention is paid to the eutectic transformation [12–15] and peritectic

---

transformation [16–20], which commonly occur during the solidification process. Karma [21] and Wheeler et al. [22] proposed early models aiming to extend the phase-field approach to simulate the eutectic transformation during alloy solidification. In these models, a dual phase-field model is used to describe the solid and liquid phases. However, these models are restricted to emulate the phase transformation between three phases. To solve this problem, a multi-phase model was developed in which an individual phase-field parameter φ_α is used to describe each phase [23–25]. Nestler and Wheeler formulated a phase-field approach based on interpolating the free energy density to study eutectic and peritectic transition in a binary alloy [26]. According to the fact that a phase transformation is attributed to the difference in the grand potentials between phases, Choudhury and Nestler reformulated a multi-phase-field model based on the grand potential functional [27]. By using this model, Steinmetz et al. investigated and predicted the undercooling-spacing-velocity relationship for complex pattern arrangements via 2-D and 3-D simulations [28]. Kellner et al. studied the influence of nucleation on the morphological evolution of eutectic colony in NiAl-34Cr [29]. Moreover, Tu et al. explored the eutectic growth in combination with solid–solid boundary anisotropy and analyzed its influence on steady and unsteady lamellar morphologies [30]. In the above mentioned studies, distinct microstructures are obtained under different solidification conditions. In the current work, we investigate the microstructural evolution of eutectic lamellae in Mo-Si-Ti alloy under different supersaturations of melt and with various lamellar spacings by using phase-field modeling. The aim is to construct a microstructure selection map for different growth morphologies. Moreover, the understanding of the influence of interfacial energy on the solidification morphology, especially from experimental studies, is considerably limited, since an accurate measurement of interfacial energy is almost impossible in experiments. The role of interfacial energy in solidification morphology will be studied in the present work by simulations.

The lamellar microstructure of Ti(Mo)$_5$Si$_3$ and β(Mo,Si,Ti) can also form via a four-phase reaction. Based on the organic alloy solidification experiments [31], Podolinsky et al. proposed a two-step eutectic formation mechanism: initially two different phases nucleate independently in the melt and then the eutectic structures form after the neighboring nuclei contact with each other. In analogy with this eutectic mechanism, it is very likely that the four-phase reaction consists of following steps: (i) Two solid phases (Ti(Mo)$_5$Si$_3$ and β(Mo,Si,Ti)) nucleate at the surface of Mo(Ti)$_3$Si independently. (ii) Two peritectic transitions occur in the vicinity of two triple junctions, namely L/Ti(Mo)$_5$Si$_3$/Mo(Ti)$_3$Si and L/β(Mo,Si,Ti)/Mo(Ti)$_3$Si. When Ti(Mo)$_5$Si$_3$ and β(Mo,Si,Ti) are close together, the four-phase reaction takes place subsequently. (iii) The four-phase reaction ends after these two phases contact with each other and the eutectic transformation happens. Therefore, the lamellae microstructure resulting from the combined effect of these reactions exhibits differences compared with that formed in a primary eutectic transformation. In the recent decades, multi-phase-field (MPF) method is employed to investigate the morphological evolution during the solidification process, such as ternary eutectic transformation [32–34]. Rahul et al. studied the microstructural evolution in the solidification of undercooled high entropy alloys by using MICRESS [35]. In addition, MPF method is widely applied for the study of grain growth. Using the same MPF approach, Park et al. investigated the epitaxial effect on the grain structure of an additively manufactured AlSi10Mg alloy [36]. Apel et al. explored the motion of grain boundary under the particle pinning effect [37]. Eiken proposed a precise analytical solution to the tri-crystal problem and predicted anisotropic grain growth by MPF simulations [38]. However, there is a paucity of research discussing the quasi-peritectic four-phase reaction, which is likely due to the following reasons: (i) the transient accomplishment of the four-phase reaction. (ii) More attention is paid to the lamellar microstructure caused by the eutectic transformation rather than the similar lamellar microstructure

produced by the quasi-peritectic four-phase reaction. (iii) The complexity caused by the potential several phase transitions. Kundin et al. [39] scrutinized a four-phase reaction in Al-Cu-Ni system. They focused on the effect of heterogeneous nucleation of fourth phase on the final morphology. The microstructural evolution of lamellae produced by four-phase reaction and the differences of lamellae growth between eutectic transformation and four-phase reaction have not yet been examined. Moreover, from results in experiments, some lamellar pairs are observed to show a bending growth at the surface of Mo(Ti)$_3$Si, as marked by a red circle in Fig. 1(a). The mechanism behind this phenomenon is unknown and worth being explored in detail.

In the present work, we cast light on the lamellae growth during a eutectic transformation and a four-phase reaction in Mo-Si-Ti alloy by using phase-field method. The objective of our research is to explore the influence of different solidification conditions on the lamellae microstructure in these two distinct phase transformation processes. In the modeling section, we present a 3-D phase-field model formulation with an anti-trapping current, coupled with the diffusion equation, to simulate the occurrence of phase transitions and the growth of intermetallic compounds. By using this phase-field method, we study the evolution of the lamellar pair Ti(Mo)$_5$Si$_3$ and β(Mo,Si,Ti) in 2-D and 3-D under different melt supersaturations and with various lamellar spacings, in both eutectic transformation and four-phase reaction. In the results section of eutectic transformation, we construct a microstructure selection map via systematic study of the lamellar spacing and the composition of Mo. Moreover, we scrutinize the influence of solid–liquid interfacial energy on the solidification morphology. In the part of four-phase reaction, we obtain lamellae microstructure differing from that in eutectic transformation. In addition, a tilt lamellae microstructure is observed in both phase transformation processes (see Fig. 1(b)). A qualitative investigation on this phenomenon will be provided in this work by phase-field simulations.

2. Phase-field model

In the present study, a phase-field model with the grand-potential formulation, which is proposed by Choudhury and Nestler [40], is used to investigate the microstructural evolution during solidification process. For an N-phase and K-component system, the bulk free energy density of the phase α is formulated as

$$f^\alpha = f^\alpha(c_1^\alpha, \ldots, c_k^\alpha, \ldots, 1 - \sum_{i=1}^{K-1} c_i^\alpha), \alpha \in [1, N], k \in [1, K]. \tag{1}$$

The diffusion potential for the α phase in this system with $K - 1$ independent components [25,41] is written in terms of the chemical potential as:

$$\mu_k^\alpha = \frac{\delta f^\alpha}{\delta c_k^\alpha} = \frac{\partial f^\alpha}{\partial c_k^\alpha} - \frac{\partial f^\alpha}{\partial c_K^\alpha} \tag{2}$$

It should be noted that this deduction of diffusion potential is applicable for substitutional systems. For interstitial systems, an adapted set of independent concentration variables should be considered similarly as proposed in [42]. The grand chemical potential is given by the following equation:

$$\Psi^\alpha(\mu) = f^\alpha(c^\alpha(\mu)) - \langle \mu^\alpha, c^\alpha \rangle, \tag{3}$$

where the concentration vector is defined as $c^\alpha = (c_1^\alpha, \ldots, c_{K-1}^\alpha)$ and the diffusion potential vector is written as $\mu^\alpha = (\mu_1^\alpha, \ldots, \mu_{K-1}^\alpha)$. When the phases are in thermodynamic equilibrium, the diffusion potential of each phase is equal to each other, hence the diffusion potential vector can be described as $\mu^\alpha = \mu = (\mu_1, \ldots, \mu_{K-1})$. The mathematical symbol $\langle , \rangle$ represents a scalar product.

In this model, we introduce an order parameter φ_α to represent the local volume fraction of the α phase, whose value characterizes the phase state of the system temporally and spatially. In addition, a diffuse interface is used to separate two distinct phases α and β. Therefore, we
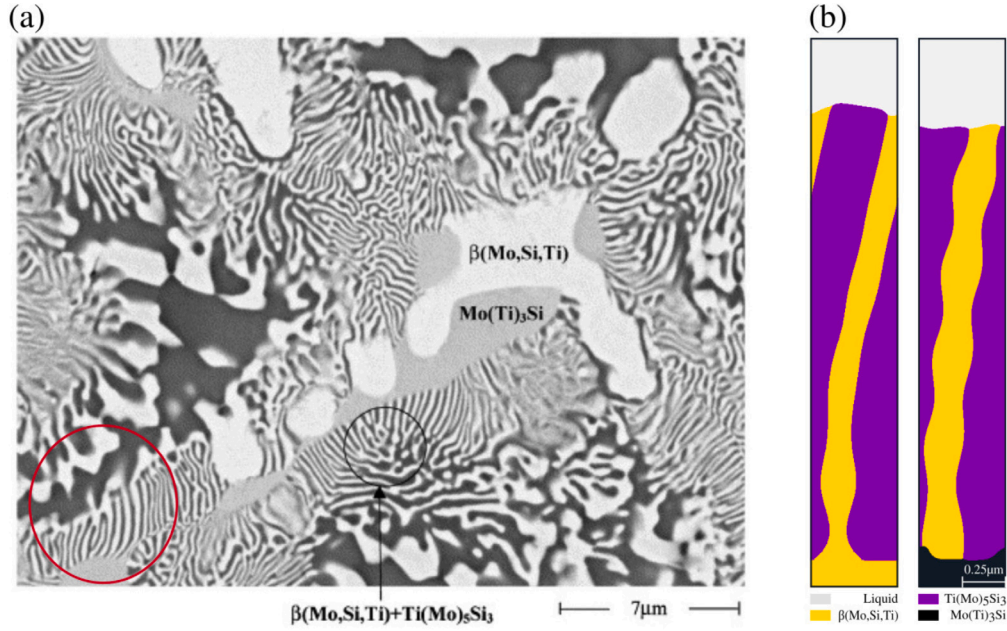
Fig. 1. (a) A back scattered image of the as-cast microstructure of the $Mo_{40}Si_{20}Ti_{40}$ alloy. Reprinted from [6]. (b) The simulation results of a bending growth of lamellae, as part of the present work.

set the order parameter $\varphi_\alpha = 1$, $0 < \varphi_\alpha < 1$, $\varphi_\alpha = 0$ in the bulk phase α, in the diffuse interface, and in other phases, respectively. The phase-field vector $\boldsymbol{\varphi} = (\varphi_1, \ldots, \varphi_N)$ is applied to characterize the phase state of the system. The grand chemical potential in the diffuse interface is interpolated in terms of the individual phases as

$$\Psi(\boldsymbol{\varphi}, \boldsymbol{\mu}) = \sum_{\alpha=1}^{N} \Psi^\alpha(\boldsymbol{\mu}) h(\varphi_\alpha), \tag{4}$$

where $h(\varphi_\alpha)$ is a cubic interpolation function defined as $h(\varphi_\alpha) = \varphi_\alpha^2(3 - 2\varphi_\alpha)$ and satisfies $h(0) = 0$ and $h(1) = 1$. With the aid of Eq. (3), we differentiate both sides of Eq. (4) with respect to μ_i yielding

$$c(\boldsymbol{\varphi}, \boldsymbol{\mu}) = \sum_{\alpha=1}^{N} c^\alpha(\boldsymbol{\mu}) h(\varphi_\alpha), \tag{5}$$

where the concentration vector is defined as $c = (c_1, \ldots, c_{K-1})$.

In accordance with the basic thermodynamic law, the fundamental idea of using the phase-field method to illustrate the phase transition process in a multiphase system is such as to minimize the grand potential functional $d\Omega/dt \leq 0$, which is achieved with the following formulation:

$$\Omega(\boldsymbol{\varphi}, \boldsymbol{\mu}) = \int_V \left[\epsilon a(\boldsymbol{\varphi}, \nabla \boldsymbol{\varphi}) + \frac{1}{\epsilon} w(\boldsymbol{\varphi}) + \Psi(\boldsymbol{\varphi}, \boldsymbol{\mu}) \right] dx. \tag{6}$$

Here, V is the volume occupied by the system, and ϵ is a length parameter, which determines the width of the diffuse interface.

The first term in Eq. (6) represents the gradient energy density that is formulated as

$$a(\boldsymbol{\varphi}, \nabla \boldsymbol{\varphi}) = \sum_{\alpha < \beta} \gamma_{\alpha\beta} [a_{\alpha\beta}(\boldsymbol{q}_{\alpha\beta})]^2 |\boldsymbol{q}_{\alpha\beta}|^2, \tag{7}$$

where $\gamma_{\alpha\beta}$ is a coefficient defining the surface energy of the $\alpha - \beta$ interface, and $\boldsymbol{q}_{\alpha\beta}$ is the generalized asymmetric gradient vector, which is written as: $\boldsymbol{q}_{\alpha\beta} = \varphi_\alpha \nabla \varphi_\beta - \varphi_\beta \nabla \varphi_\alpha$. Here, the anisotropy of all phases is not taken into consideration, hence $a_{\alpha\beta}(\boldsymbol{q}_{\alpha\beta})$ is set as 1.

The second term in Eq. (6) is an obstacle potential, which is expressed as

$$w(\boldsymbol{\varphi}) = \begin{cases} \frac{16}{\pi^2} \sum_{\alpha < \beta} \gamma_{\alpha\beta} \varphi_\alpha \varphi_\beta + \sum_{\alpha < \beta < \delta} \gamma_{\alpha\beta\delta} \varphi_\alpha \varphi_\beta \varphi_\delta & \boldsymbol{\varphi} \in G \\ +\infty & else, \end{cases} \tag{8}$$

where G is the Gibbs simplex and defined as $G = \{ \boldsymbol{\varphi} \in \mathbb{R}^N : \sum_\alpha \varphi_\alpha = 1, \varphi_\alpha \geq 0 \}$.

Here, the higher order term $\gamma_{\alpha\beta\delta}$ suppresses spurious contributions of third phases in the binary interfaces. The temporal phase-field evolution equation is derived by the variational approach and writes as

$$\tau_{\alpha\beta} \epsilon \frac{\partial \varphi_\alpha}{\partial t} = \underbrace{\epsilon \left[\frac{\partial a(\boldsymbol{\varphi}, \nabla \boldsymbol{\varphi})}{\partial \varphi_\alpha} - \nabla \cdot \frac{\partial a(\boldsymbol{\varphi}, \nabla \boldsymbol{\varphi})}{\partial \nabla \varphi_\alpha} \right] - \frac{1}{\epsilon} \frac{\partial w(\boldsymbol{\varphi})}{\partial \varphi_\alpha} - \left[\Psi^\alpha(\boldsymbol{\mu}) - \Psi^\beta(\boldsymbol{\mu}) \right] h'(\varphi_\alpha) - \Lambda,}_{=:rhs_\alpha}$$

$$\alpha = 1, \ldots, N, \beta \neq \alpha. \tag{9}$$

The Lagrange multiplier Λ is defined as

$$\Lambda = \frac{1}{N} \sum_{\alpha=1}^{N} rhs_\alpha, \tag{10}$$

to ensure $\sum_{\alpha=1}^{N} \varphi_\alpha = 1$. The modeling parameter $\tau_{\alpha\beta}$ is a relaxation constant at the α/β interface and calculated based on the deviation from [40]. Furthermore, the total amount of solute in the system is conserved. Therefore, we introduce a diffusion equation, which follows Fick's law. As the flux in the diffuse interface of phase-fields differ from the sharp interface limit, an anti-trapping current is added in this solute conservation equation. The evolution equation for the concentration fields is derived as [40,43]

$$\frac{\partial c}{\partial t} = -\nabla \cdot \boldsymbol{J} = \nabla \cdot \left[\boldsymbol{D} \nabla c - \boldsymbol{J}_{at} \right] = \nabla \cdot \left[\boldsymbol{M}(\boldsymbol{\varphi}, \boldsymbol{\mu}) \nabla \boldsymbol{\mu} - \boldsymbol{J}_{at} \right], \tag{11}$$

where $\boldsymbol{M}(\boldsymbol{\varphi}, \boldsymbol{\mu}) = \sum_{\alpha=1}^{N} \boldsymbol{M}^\alpha(\boldsymbol{\varphi}, \boldsymbol{\mu}) h(\varphi_\alpha)$ is the mobility. The mobility of atoms in α phase $\boldsymbol{M}^\alpha$ is defined as

$$\boldsymbol{M}^\alpha = \frac{\boldsymbol{D}^\alpha}{\frac{\partial \boldsymbol{\mu}}{\partial c^\alpha}}, \tag{12}$$

where $\boldsymbol{D}^\alpha$ is the chemical diffusivity matrix in α phase. It should be noted that we only consider the chemical diffusion in the isothermal solidification process. Other types of diffusion, such as thermal-induced diffusion [44,45], electrical-induced diffusion [46,47], or stress-induced

diffusion [48], are not taken into account. In this paper, we state the result as the anti-trapping current in the phase-field simulation and refer to another paper for details of the asymptotics and derivation [40]. The anti-trapping current is defined as

$$\boldsymbol{J}_{at} = \frac{\pi\epsilon}{4}\sum_{\alpha=1}^{N}\frac{h(\varphi_\alpha)(1-h(\varphi_\alpha))}{\sqrt{\varphi_\alpha^0(1-\varphi_\alpha^0)}}\frac{\partial\varphi_\alpha}{\partial t}\left(\frac{\nabla\varphi_\alpha}{|\nabla\varphi_\alpha|}\cdot\frac{\nabla\varphi_L}{|\nabla\varphi_L|}\right)\left((c^L(\boldsymbol{\mu})-c^\alpha(\boldsymbol{\mu}))\otimes\frac{\nabla\varphi_\alpha}{|\nabla\varphi_\alpha|}\right),$$

(13)

where φ_α^0 is the lowest order solution of the phase-field equation, c^L and c^α are the concentrations in liquid and solid phases, respectively. According to Eq. (5), the time derivative of the concentration is written as

$$\frac{\partial \boldsymbol{c}}{\partial t} = \sum_{\alpha=1}^{N} c^\alpha(\boldsymbol{\mu})\frac{\partial h(\varphi_\alpha)}{\partial t} + \sum_{\alpha=1}^{N}\frac{\partial c^\alpha(\boldsymbol{\mu})}{\partial t}h(\varphi_\alpha)$$

$$= \sum_{\alpha=1}^{N} c^\alpha(\boldsymbol{\mu})h'(\varphi_\alpha)\frac{\partial\varphi_\alpha}{\partial t} + \sum_{\alpha=1}^{N}\frac{\partial c^\alpha}{\partial\boldsymbol{\mu}}h(\varphi_\alpha)\frac{\partial\boldsymbol{\mu}}{\partial t}.$$

(14)

Through a combination of Eqs. (11) and (14), the evolution equation for the diffusion potential is formulated as

$$\frac{\partial \boldsymbol{\mu}}{\partial t} = \left[\sum_{\alpha=1}^{N}\frac{\partial c^\alpha(\boldsymbol{\mu})}{\partial\boldsymbol{\mu}}h(\varphi_\alpha)\right]^{-1}$$

$$\cdot\left[(\nabla\cdot(\boldsymbol{M}(\boldsymbol{\varphi},\boldsymbol{\mu})\nabla\boldsymbol{\mu}-\boldsymbol{J}_{at})) - \sum_{\alpha=1}^{N} c^\alpha(\boldsymbol{\mu})h'(\varphi_\alpha)\frac{\partial\varphi_\alpha}{\partial t}\right].$$

(15)

In the following discussion, we simulate the growth of lamellar pair (Ti(Mo)$_5$Si$_3$ and β(Mo,Si,Ti) phases) with different melt compositions and their evolution with various lamellar spacing during a eutectic transformation and a four-phase reaction. The interface thickness is set to be 0.06 μm in order to keep the simulation stable. The reason for this setting is explained in supplementary document. For the eutectic transformation, we establish a cooling situation at fixed composition along the equilibrium phases in the phase diagram and initially fill a semicircular Ti(Mo)$_5$Si$_3$ nucleus at the interface between the liquid and β(Mo,Si,Ti) phases. For the four-phase reaction, two semicircular particles Ti(Mo)$_5$Si$_3$ and β(Mo,Si,Ti) are placed at some distance next to each other on top of the Mo(Ti)$_3$Si phase and surrounded by the liquid. The other simulation parameters are listed in Table 1. We use the following way to obtain the diffusion coefficients for the lack of direct experimental data in Mo-Si-Ti system. According to Ref. [49], the diffusion coefficients of molybdenum and tantalum in the melt are related to their melting points and show almost the same dependence on the homologous temperature T$_h$, which is defined as T$_h = T/T_m$ (T$_m$ is the melting temperature). Based on this result, we assume that titanium and silicon have similar dependence on T$_h$, and calculate their diffusion coefficients in melt for the present study by D$_{Ti}^L$ =D$_{Si}^L$ =6.6×10^{-9} m^2 s^{-1} (2216 K). Through comparing D$_{Ti}^L$ with the data 5.3×10^{-9} m^2 s^{-1} (2000 K) from [50], it is reliable to set the diffusion coefficient for all three components (Mo, Si, Ti) in liquid phase with the same value 6.6×10^{-9} m^2 s^{-1}. For the diffusion coefficients in solid phases, we use the value based on the data from [51]. In Ref. [51], the self-diffusion of titanium D$_{Ti}^s$ and impurity diffusion coefficients of molybdenum D$_{Mo}^i$ in β-Ti matrix with body-centered cubic structure are calculated, which has the same crystalline structure as the β(Mo,Si,Ti) phase. After a linear extrapolation to the temperature 2216 K, we obtain D$_{Ti}^s$ = 1×10^{-9} m^2 s^{-1} and D$_{Mo}^i$ = 1×10^{-10} m^2 s^{-1} approximately. Due to the great difference in the diffusion coefficient between liquid and solid phases and the fact that the phase transformation in the present study is caused by a supersaturation in liquid, we set the diffusion coefficients in all solid phases of all components with the same value for simplification. In addition, assumptions referring to the common interfacial energy 1 J m^{-2} in alloy system [52,53] are made to assign a suitable value for the interfacial energies between each two phases.

Table 1
Parameters for the phase-field simulations.

Symbol	Description	Value
Δt	Time step	0.5×10^{-7} s
Δx	Space step	0.5×10^{-8} m
$\sigma_{i/j}$	Interfacial energy	1 J m^{-2}
D$_{Mo}^L$	Diffusion coefficient of Mo in the liquid phase	6.6×10^{-9} m^2 s^{-1} [49]
D$_{Ti}^L$	Diffusion coefficient of Ti in the liquid phase	6.6×10^{-9} m^2 s^{-1}
D$_{Si}^L$	Diffusion coefficient of Si in the liquid phase	6.6×10^{-9} m^2 s^{-1}
D$_{Mo}^S$	Diffusion coefficient of Mo in the solid phases	0.5×10^{-9} m^2 s^{-1} [51]
D$_{Ti}^S$	Diffusion coefficient of Ti in the solid phases	0.5×10^{-9} m^2 s^{-1} [51]
D$_{Si}^S$	Diffusion coefficient of Si in the solid phases	0.5×10^{-9} m^2 s^{-1}

Note: i, j = liquid, Ti(Mo)$_5$Si$_3$, β(Mo,Si,Ti), Mo(Ti)$_3$Si.

The influence of different interfacial energies on the morphological evolution is investigated in a forthcoming paper.

3. Ternary phase diagram of Mo-Si-Ti system

According to the thermodynamic database published in Ref. [54], Ti(Mo)$_5$Si$_3$ and β(Mo,Si,Ti) are produced simultaneously by a four-phase reaction involving liquid and Mo(Ti)$_3$Si phase at the temperature T$_{4p}$ = 2221 K, L + Mo(Ti)$_3$Si → Ti(Mo)$_5$Si$_3$ + β(Mo,Si,Ti). When the temperature is lower than T$_{4p}$, a eutectic transformation takes place forming the lamellae of Ti(Mo)$_5$Si$_3$ and β(Mo,Si,Ti), L → Ti(Mo)$_5$Si$_3$ + β(Mo,Si,Ti). The formation and development of the lamellae Ti(Mo)$_5$Si$_3$ and β(Mo,Si,Ti) via the four-phase reaction and the eutectic transformation will be focused in this work by phase-field simulations. The corresponding thermodynamic database (tdb-file) is provided by the authors of [6,54] (Y. Du) and used in present work. The dataset will be cross-checked in this work by calculating isothermal sections, temperature-sections, liquidus surface, and corresponding thermodynamic functions. In the following sections, we use the notations TS, MS, and β to represent Ti(Mo)$_5$Si$_3$, Mo(Ti)$_3$Si and β(Mo,Si,Ti) phase, respectively. For the coupling of CALPHAD database with the phase-field model, we use a parabolic function to describe the free energy density of each phase in the present study [55–57]. This coupling approach is chosen for the following two reasons: (a) In CALPHAD database, the free energy density f^α of a single phase is written by a Redlich–Kister polynomial [58] in the form of $\sum_{i=1} c_i^\alpha \ln c_i^\alpha + \sum_{i,j}^{K} c_i^\alpha c_j^\alpha$. In the simulation, we have to calculate c^α as a function of the diffusion potential $\boldsymbol{\mu}$ as well as the derivative of c^α with respect to $\boldsymbol{\mu}$ in Eq. (15). For the free energy density written in CALPHAD approach, $c^\alpha(\boldsymbol{\mu})$ has to be solved implicitly, while $c^\alpha(\boldsymbol{\mu})$ is an explicit function when the free energy is written in a parabolic form. The latter one can significantly increase the computational efficiency. For a detailed comparison of the computational effort between these two approaches, we refer to Ref. [59], where an acceleration of about 10 times is achieved via the parabolic approximation. (b) The mobilities are related with the second derivative of the free energy density with respect to the composition. However, the stoichiometric phase in CALPHAD database has a fixed composition and thus the value of the second derivative is missing in the CALPHAD database. In order to solve this problem, we assume a solid solubility in the stoichiometric phase. This assumption has been proven by several experiments. For the two considered stoichiometric solid phases in the present study, the silicon content in TS phase is not fixed at 0.375 but varies around the experimental value [60,61]. For the MS phase, a deviation of silicon concentration from 0.25 has also been observed [61]. Therefore, the assumption of a certain solid solubility in these two phases is reasonable. In the following study, the free energy density of liquid phase is expressed by the following function:

$$f^L = a(T)^L c_{Mo}^2 + b(T)^L c_{Mo} + d(T)^L + e(T)^L c_{Ti}^2 + g(T)^L c_{Ti} + h(T)^L c_{Mo}c_{Ti},$$

(16)

Table 2
Parameters for the fitted free energy functions.

Phase	a	b	d	e	g	h	n
Liquid	1.994	−1.787	−1.264	2.382	−2.617	3.644	—
Ti(Mo)$_5$Si$_3$	1.237	−0.022	−2.015	—	—	—	10
Mo(Ti)$_3$Si	1.657	−0.349	−1.802	—	—	—	10
β(Mo,Si,Ti)	1.051	−0.544	−1.541	—	—	—	1000

and fitted by the least square method in the temperature range from 2196 K to 2219 K based on the thermodynamic data in CALPHAD database. The intermetallic phase TS is exactly stoichiometric with a constant Si concentration 0.375 in CALPHAD database. Presently, we model a temperature dependent of silicon solubility in TS phase by the following expression

$$f^{TS} = \left[a(T)^{TS}(c_{Mo}+b(T)^{TS})^2 + d(T)^{TS}\right] + n^{TS}a(T)^{TS}(0.625-c_{Mo}-c_{Ti})^2.$$
(17)

The formulation of Eq. (17) consists of two parts. The first part is fitted by the least square method based on the data from CALPHAD and depicts the free energy density as a function of Mo concentration c_{Mo}. The second part models a temperature dependent solubility of Si in the TS phase, differing from other fitting methods. In the similar manner, the free energy densities of MS and β phases are written as:

$$f^{MS} = \left[a(T)^{MS}(c_{Mo}+b(T)^{MS})^2 + d(T)^{MS}\right] + n^{MS}a(T)^{MS}(0.75-c_{Mo}-c_{Ti})^2.$$
(18)

and

$$f^{\beta} = \left[a(T)^{\beta}(c_{Mo}+b(T)^{\beta})^2 + d(T)^{\beta}\right] + n^{\beta}a(T)^{\beta}(0.9797-c_{Mo}-c_{Ti})^2.$$
(19)

The solubility of the silicon in the β phase varies between 0 and 0.04 in the considered temperature range. The variation of the temperature dependent solubility is achieved by the n^{β}-related term. For an illustration of the thermodynamic consistency of the fitting method, the free energy densities of liquid phase as a function of c_{Mo} for four exemplary temperatures are shown in Fig. 2(a)–(d), respectively. Fig. 2(e) illustrates the free energy densities of TS phase for these four temperatures, while the free energy densities of MS and β phases are depicted in Fig. 2(f) and (g), respectively. The filled symbols represent the data from CALPHAD database and the fitted functions are depicted by solid lines. The good consistency between the fitted free energy and the CALPHAD dataset demonstrates the capability of the present fitting method in the considered temperature range. After the calibration of the temperature and composition dependent thermodynamic data with respect to the CALPHAD database, we apply this result to the growth of the eutectic lamellae during isothermal solidification at the temperature $T = 2216$ K. At this temperature, all unknowns in the free energy functions are listed in Table 2. The free energy landscapes of the considered phases are shown in Fig. 3(a)–(d) at the temperature of $T = 2216$ K. For a better visualization, the free energy density of the liquid phase along a particular trajectory in the ternary plot is shown in Fig. 3 as an example. Fig. 3(e) illustrates the fitted free energy density for the liquid phase as a function of the concentration of molybdenum c_{Mo} by violet points. In the similar manner, the relationship between the fitted free energy and the concentration of titanium c_{Ti} is portrayed in Fig. 3(f). In Fig. 3(e) and (f), data from CALPHAD database are represented by a gray line to verify the reliability of the fitted function for liquid phase.

To further prove the thermodynamic consistency of the present method, we calculate the free energy density f/E^*, the diffusion potential with respect to molybdenum μ_{Mo}/E^* and titanium μ_{Ti}/E^*, and the grand chemical potential Ψ/E^* of the liquid phase, in comparison with

the CALPHAD database, for six considered compositions, as listed in Table 3. In addition, we also calculated the equilibrium concentrations between three solid phases as well as the corresponding values f/E^* and Ψ/E^*, and compared them with the data from CALPHAD, as listed in Table 4. Fig. 4(a) shows the reconstructed isothermal section of L-TS-MS-β phase region in the Mo-Si-Ti system at temperature $T = 2216$ K. The violet, blue, yellow, and red lines correspond to the liquid, TS, MS, and β phases, respectively. The equilibrium concentrations calculated by the fitted free energy functions are illustrated by dashed lines. The data from CALPHAD database [54] is represented by solid lines for a comparison. As shown in Fig. 4(a), the β single phase region calculated by the parabolic free energy function almost overlaps with the one from CALPHAD. It implies that our fitted free energy density of the β phase in the parabolic form reproduces the silicon solubility in the CALPHAD database. As the TS and MS phases both are exactly stoichiometric in the CALPHAD database a direct reproduction of the silicon solubility in these two phases is almost impossible. In the current study, the calculated silicon concentrations in the TS and MS phase are 0.363 ± 0.036 and 0.243 ± 0.023, respectively, which are within the range of the experimental observation [60,61]. However, a more quantitative calculation of the solubility in the TS and MS phases is challenging due to the lack of the sufficient experimental data.

The initial mole fractions of Mo, Ti, and Si in the TS, β, and MS phases are indicated by the black circles in Fig. 4(a). For the phases TS and β, their initial composition deviates from the equilibrium concentration providing a solutal driving force for the phase transformation in the present study. The initial composition of MS phase is the equilibrium concentration of three-phase eutectoid. It is noteworthy that the difference between the fitted value and the data from CALPHAD database is caused by the assumption of the solute solubility in stoichiometric phases. The black triangles 1 and 2 in Fig. 4(a) depict the L-TS-β and MS-TS-β phase region, respectively, corresponding to the triangles 1 and 2 in the isothermal section of Mo-Si-Ti phase diagram in Fig. 4(b). A comparison between Fig. 4(a) and (b) reveals that the fitted free energy functions can be used in the phase-field simulations to describe the four-phase reaction and the three-phase eutectic transformation quantitatively.

4. Simulation results and discussion

According to the previous study [6], the formation of the lamellar pair (TS and β) occurs at the surface of two different particles: the primary solidified β phase and the MS phase. The former one is caused by a eutectic transformation (L → Ti(Mo)$_5$Si$_3$ + β(Mo,Si,Ti)) and the latter one arises from a four-phase reaction (L + Mo(Ti)$_3$Si → Ti(Mo)$_5$Si$_3$ + β(Mo,Si,Ti)). Aiming to explore the influencing factors of the microstructure of the lamellar pair (TS and β) formed by different phase transition processes, we simulate isothermal eutectic transformation as well as the four-phase reaction of Mo-Si-Ti alloy by using the phase-field model in 2-D and 3-D domains. For both phase transformation processes, we shed light on the microstructural evolution of the lamellar pair with different supersaturations in liquid and with different lamellar spacings. Since the 3-D simulations are closer to the reality, we simulate the rod eutectic growth in 3-D domains to clarify the influence of neighboring particles.

In the following study, the Neumann boundary condition for all fields is applied at the solidified end of the domain. An infinite domain perpendicular to the solidification front is modeled by periodic boundary condition. At the liquid end of the domain, a constant flux of melt is realized by the Dirichlet boundary condition. Considering this infinite flux of melt, the negligible evolution of the solidified phases, and the reduction in the computational effort, we only simulate the region around the solidification front. This is achieved by a moving window technique [62], which is controlled by the height of solidification front.
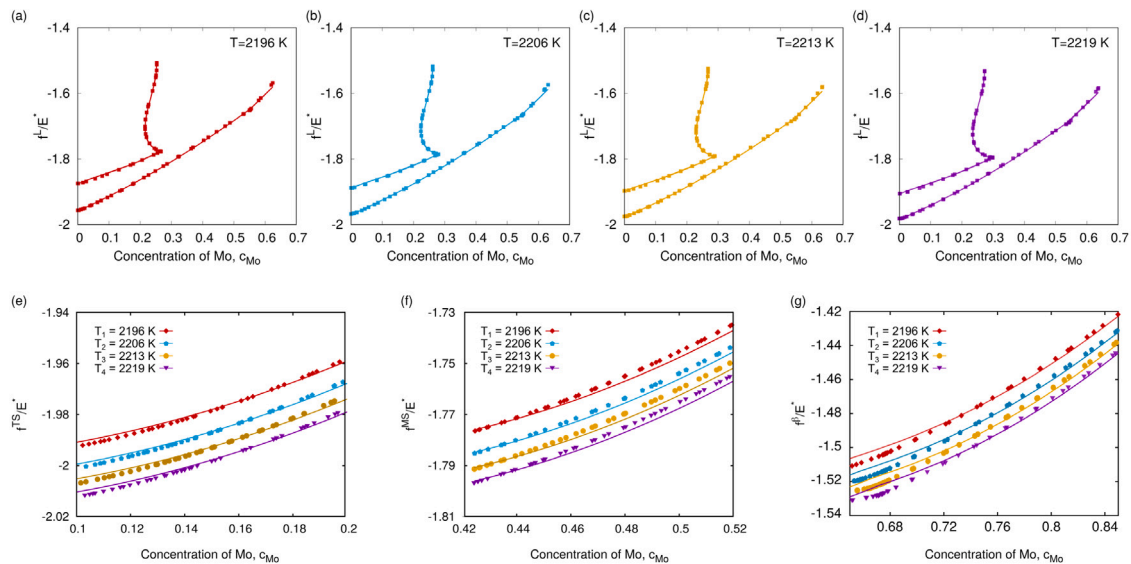
Fig. 2. (a)–(d) The free energy densities of liquid phase as a function of c_{Mo} for four exemplary temperatures, respectively. (e)–(g) The free energy densities for these four temperatures of Ti(Mo)$_5$Si$_3$, Mo(Ti)$_3$Si, and β(Mo,Si,Ti) phases, respectively.
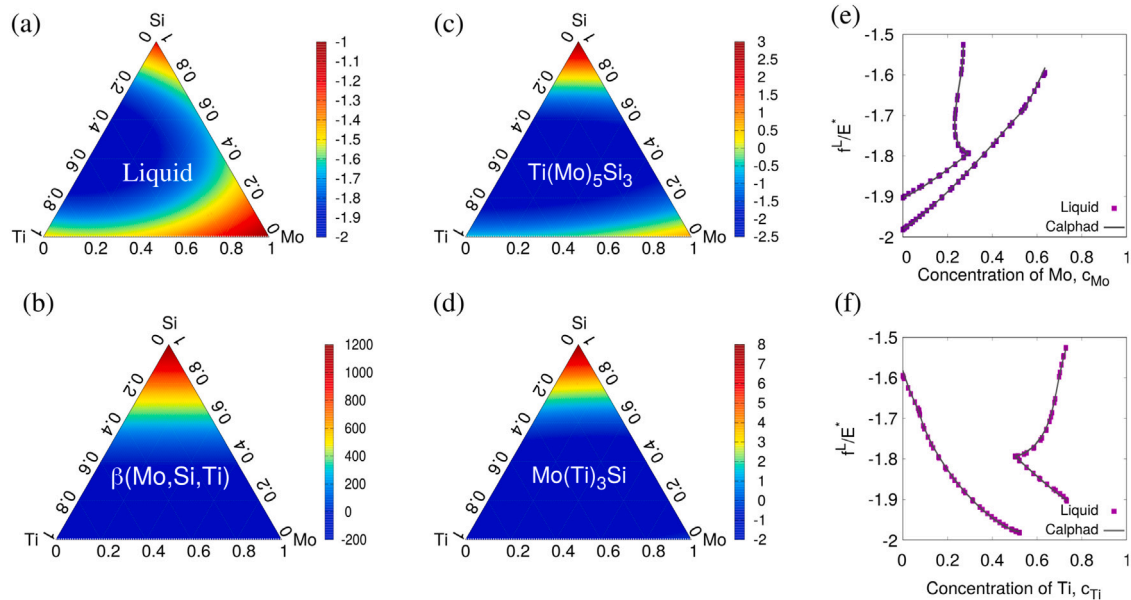
Fig. 3. (a)–(d) The free energy density landscape of liquid, β(Mo,Si,Ti), Ti(Mo)$_5$Si$_3$, and Mo(Ti)$_3$Si phase, respectively, based on the fitted free energy functions in Eqs. (16)–(19) (red: high, blue: low). (e) and (f) display the free energy density f/E^* for the liquid phases at the temperature $T = 2216$ K as a function of concentration of molybdenum and of concentration of titanium, respectively, where $E^* = 1 \times 10^{10}$ J/m^3. The dashed curves represent the fitted free energy functions and the black lines corresponding to the data from CALPHAD database.

Table 3
The calculated free energy density f/E^*, diffusion potentials of molybdenum μ_{Mo}/E^* and titanium μ_{Ti}/E^*, as well as grand chemical potential Ψ/E^* for liquid phase and the corresponding experimental data from [54].

Composition	f/E^*			μ_{Mo}/E^*			μ_{Ti}/E^*			Ψ/E^*		
	Fitted	Exp.	Error	Fitted	Exp.	Error	Fitted	Exp.	Error	Fitted	Exp.	Error
23Mo-56Ti-21Si	−1.819	−1.819	0	1.170	1.224	4.35%	0.889	0.951	6.48%	−2.587	−2.632	1.72%
24Mo-55Ti-21Si	−1.817	−1.817	0	1.174	1.225	4.16%	0.878	0.948	7.35%	−2.581	−2.631	1.90%
25Mo-54Ti-21Si	−1.814	−1.814	0	1.177	1.226	3.98%	0.867	0.945	8.22%	−2.576	−2.629	2.02%
26Mo-53Ti-21Si	−1.810	−1.809	0.06%	1.181	1.228	3.86%	0.856	0.938	8.75%	−2.571	−2.626	2.10%
28Mo-51Ti-21Si	−1.804	−1.799	0.28%	1.188	1.231	3.54%	0.833	0.923	9.74%	−2.561	−2.619	2.22%
30Mo-49Ti-21Si	−1.796	−1.794	0.13%	1.195	1.232	3.04%	0.811	0.916	11.49%	−2.552	−2.616	2.44%

Table 4

The calculated equilibrium concentration, the free energy density as well as the grand chemical potential for three solid phases and the corresponding experimental data from [54].

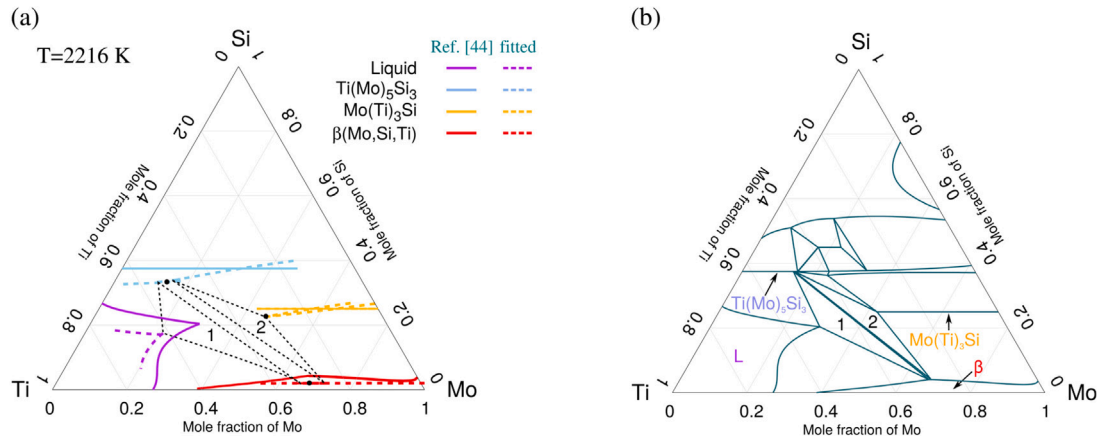|	TS				MS				β			
	c_{Mo}	c_{Ti}	f/E^*	Ψ/E^*	c_{Mo}	c_{Ti}	f/E^*	Ψ/E^*	c_{Mo}	c_{Ti}	f/E^*	Ψ/E^*
fitted	0.139	0.525	−1.980	−2.661	0.461	0.313	−1.773	−2.559	0.682	0.298	−1.521	−2.336
exp.	0.140	0.485	−1.999	−2.609	0.424	0.326	−1.794	−2.609	0.674	0.285	−1.524	−2.609
error	0.660%	8.230%	0.953%	1.964%	8.64%	3.89%	1.194%	1.923%	1.152%	4.584%	0.195%	10.485%

Fig. 4. (a) The reconstructed isothermal section of L-TS-MS-β phase region in the Mo-Si-Ti system at temperature $T = 2216$ K. (b) The isothermal section of Mo-Si-Ti phase diagram at temperature $T = 2216$ K based on the thermodynamic database [54].

4.1. 2-D simulation: Morphological evolution of lamellar pair

In this section, we focus on the growth of lamellar pair, when the TS nucleus sits on the surface of β particle. As λ increases, the radius of TS nucleus maintains at $r = 0.05$ μm, which is the critical nucleation size for TS particle under the smallest supersaturation based on the classical nucleation theory. Fig. 5(a) portrays the morphological evolution of the lamellar pair with different lamellar spacings λ. A semicircular nucleus of the TS phase is initially placed on the L-β interface. With increasing λ, three possible final morphologies are observed: (m$_i$) The engulfment of β particle by the TS phase (unstable growth mode), (m$_{ii}$) The lamellar structure with a planar TS-β interface (stable growth mode), and (m$_{iii}$) The lamellar structure with an oscillatory TS-β interface (metastable growth mode). When λ is relatively small, the distance between adjacent TS particles decreases and the growth competition between the β phase and the neighboring TS phase is more pronounced. As a result, the β particle is overgrown by the adjacent TS grains resulting in an unstable growth mode (type m$_i$). To better explore the underlying physical mechanism for the stable and metastable growth modes, we analyze the variation of the growth velocity of β phase with time. Fig. 5(b) exemplifies its growth velocity v as a function of time for the cases with lamellar spacing $\lambda = 0.4$ μm, 0.6 μm, and 0.8 μm, which are shown by the orange, green, and violet lines, respectively.

The composition of melt for all three cases is fixed at 30Mo-49Ti-21Si. For the case with $\lambda = 0.4$ μm, the growth rate of β phase converges to a constant value after the initial oscillation, whereas the growth rates for other two cases with larger λ oscillate around a particular value. With increasing lamellar spacing, the growth velocity shows a transformation from no oscillation to oscillation corresponding to the change from stable (type m$_{ii}$) to metastable (type m$_{iii}$) growth modes. The amplitude for the velocity of the oscillation increases with λ. In the present study, the eutectic transformation is caused by the supersaturation in melt, which indicates the concentration deviation in liquid from the equilibrium concentration with respect to TS- and β-phase. Hence, this phase transformation is mainly controlled by the diffusion of atoms from liquid. The whole diffusion process consists of two parts: one is the diffusion along the growth direction called

axial diffusion, the other is the diffusion perpendicular to the growth direction called lateral diffusion. Due to the constant composition of melt for the three different lamellar spacings, $\lambda = 0.4$ μm, 0.6 μm, and 0.8 μm, the variation of axial diffusion between these three cases can be ignored. For the lateral diffusion, its diffusion path increases with an enlargement in lamellar spacing. As a result, the coupling of these two diffusion processes exhibits a metastable state instead of the steady state like the case with relatively smaller λ. The underlying mechanism of this oscillation phenomenon in eutectic patterns has been investigated systematically in other papers [63–65].

In addition, we explore the influence of supersaturation in liquid on the growth of lamellar pair. The considered initial concentrations in liquid phase are 23Mo-56Ti-21Si, 24Mo-55Ti-21Si, 25Mo-54Ti-21Si, 26Mo-53Ti-21Si, 28Mo-51Ti-21Si, and 30Mo-49Ti-21Si. Here, the initial concentration of silicon in the liquid phase is constant in all six cases, hence there is only one independent component in the present study and the concentration of molybdenum c_{Mo} is used to represent the supersaturation in liquid. Fig. 5(c) portrays a regime diagram describing the three growth modes for the six considered liquid compositions. The regions marked by gray, orange, and violet correspond to the unstable (m$_i$), stable (m$_{ii}$), and metastable (m$_{iii}$) growth regions, respectively (see Fig. 5(a)). The boundaries between unstable and stable as well as between stable and metastable growth mode shift towards the direction of λ reduction as the supersaturation increases. Furthermore, the growth mode of lamellar pair for the case with a larger supersaturation in melt is more sensitive to the variation in lamellar spacing. In order to explain this finding, we compare the relationship between v and λ for the cases with $c_{Mo} = 0.24$ and 0.30, as depicted by green and violet lines in Fig. 5(d). For the case of lamellar pair with oscillatory interface, we use an average growth velocity to represent its growth rate. With an enlarging λ, the growth rate decreases for both cases, which are in accordance with the prediction of Jackson–Hunt theory for the case with large lamellar spacing [66]. For the case with $c_{Mo} = 0.24$, the growth velocity decreases slightly with increasing λ, whereas the growth velocity for the case with $c_{Mo} = 0.30$ reduces rapidly. Moreover, the growth rate in the former case is always slower than the latter case. With increasing λ, the lateral diffusion becomes weaker, whereas the
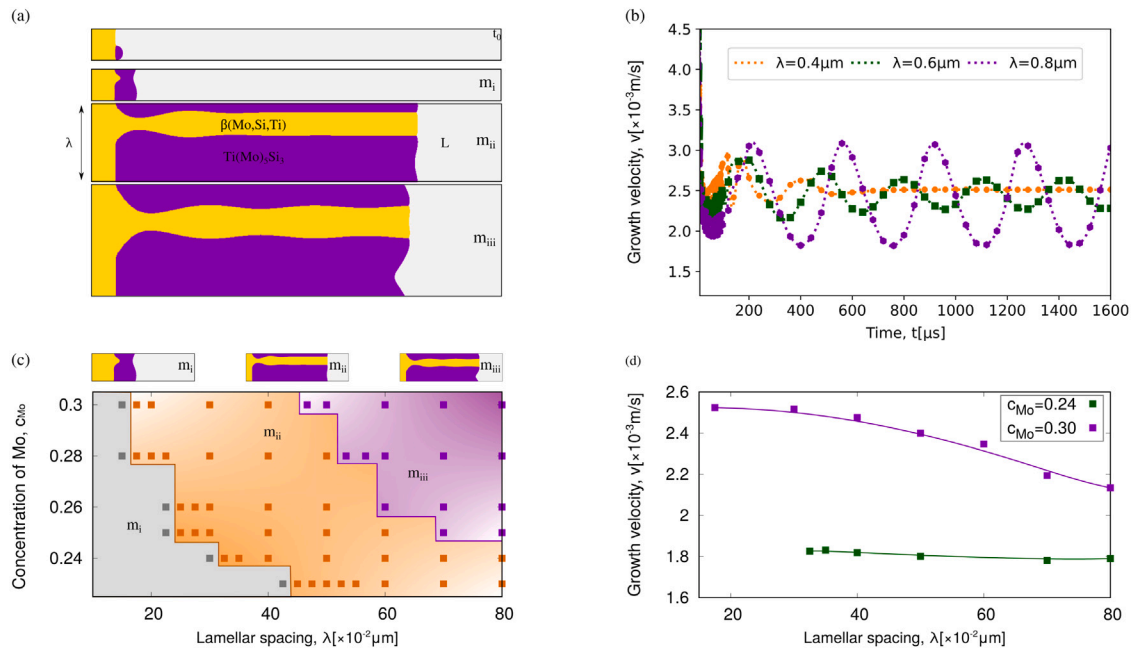
Fig. 5. (a) Three typical morphologies of the lamellar pair: (m$_i$) The engulfment of β particle by the TS phase (unstable growth mode), (m$_{ii}$) The lamellar structure with a planar TS-β interface (stable growth mode), and (m$_{iii}$) The lamellar structure with an oscillatory TS-β interface (metastable growth mode). (b) Growth velocity of β phase v as a function of time for the cases with lamellar spacing $\lambda = 0.4$ μm, 0.6 μm, and 0.8 μm, respectively. (c) The morphology regime diagram describing the three growth modes for six different liquid compositions: 23Mo-56Ti-21Si, 24Mo-55Ti-21Si, 25Mo-54Ti-21Si, 26Mo-53Ti-21Si, 28Mo-51Ti-21Si, and 30Mo-49Ti-21Si and for different lamellar spacings from 0.1–0.8 μm. (d) Growth velocity as a function of lamellar spacing λ for the cases with c$_{Mo} = 0.24$ and 0.30.

axial diffusion due to the same initial supersaturation in liquid remains almost unchanged. For small supersaturation, the axial diffusion is comparable with the lateral diffusion in a wide range of λ. In this case, the coupling of axial and lateral diffusion leads to a stable growth of the lamellar pair. In contrast, for large supersaturations, only when λ is relatively small where the lateral diffusion is pronounced. The axial diffusion is comparable with the lateral diffusion, resulting in stable growth. When λ increases, the lateral diffusion becomes weaker and cannot give rise to a steady diffusion process because of strong diffusion in the axial direction. By this way, oscillatory growth is achieved when the supersaturation and the lamellar spacing are relatively large.

4.2. 3-D simulation: Rod eutectic growth

Next, we perform 3-D simulations to compare with 2-D simulations. The additional curvature contribution in 3-D affects the microstructural evolution in the eutectic transformation, which is not considered in 2-D simulation. In addition, the effect of neighboring particles on the rod eutectic growth should also be taken into account. In this section, we investigate the eutectic phase transformation in 3-D by varying the lamellar spacing in x and z directions. The differences between 2-D simulations and 3-D simulations are discussed.

Fig. 6(a) and (b) portray side views of the morphological evolution for the cases: (i) with same lamellar spacing $\lambda_x = \lambda_z = 0.5$ μm and (ii) with different lamellar spacing $\lambda_x = 0.5$ μm and $\lambda_z = 0.7$ μm, respectively. For both cases, a hemisphere TS particle with a radius of 0.125 μm is placed initially on the surface of β phase surrounded by the melt with the same composition 26Mo-53Ti-21Si. From the side view, a stable eutectic growth at the time t$_3$ = 1540 μs is observed in case (i), whereas the elimination of β phase and the split of TS phase are shown in case (ii). A comparison of the height for the solidification front between cases (i) and (ii) at the same time shows that a larger lamellar spacing in z dimension leads to a slower axial growth in case (ii). As a result, an unstable growth in x–y plane, namely the engulfment of β phase by TS phase, is observed in case (ii), instead of the stable growth in case (i). Fig. 6(c) depicts the top view of the rod eutectic growth

corresponding to cases (i) and (ii). During this eutectic transformation, the growth of these two phases exhibits an anisotropic behavior. The results show that the morphology depends on the ratio of the lamellar distances. Due to the unequal lamellar spacing in x and z directions, these two cases show distinguish morphological evolution.

For comparison, Fig. 6(d) and (g) illustrate 2-D simulation results of two cases: (1) The lamellar structure with a planar β/TS interface, when $\lambda = 0.5$ μm and (2) the lamellar structure with an oscillatory β/TS interface, when $\lambda = 0.7$ μm, respectively. The x–y cross section of the 3D case (i) is shown in Fig. 6(e). The x–y and y–z cross sections of the 3D case (ii) are illustrated in Fig. 6(f) and Fig. 6(h), respectively. All the cross sections from 3-D simulations are through the center of TS particle. A comparison between Fig. 6(d), Fig. 6(e), and Fig. 6(f) demonstrates that the engulfment of β phase occurs in 3-D, whereas the lamellar pair is stable in 2-D. For the cases with larger lamellar spacing, the eutectic growth in 2-D exhibits an oscillatory interface between the lamellar pair (see Fig. 6(h)), while the eutectic growth in 3-D reaches a steady state after a certain time and shows lamellar structure with a planar β/T interface finally. Under the same supersaturation in liquid and with the same lamellar spacing, the eutectic growth in 3-D displays the microstructure corresponding to the cases with smaller lamellar spacing or with lower supersaturation in 2-D. Owing to that the heights of solidification front are almost identical in cases with the same simulation conditions, for instance cases shown in Fig. 6(d), (e) and (f), the axial diffusion process is almost identical for all cases. The difference between 2-D and 3-D simulations is induced by the lateral diffusion. A schematic illustration of the difference between 2-D and 3-D simulations is depicted in Fig. 7. The domain in our simulation is represented by solid lines and the adjacent domains are complemented by the dashed lines due to the periodic boundary condition. In 2-D simulations, only the diffusion flux in x direction is taken into consideration for lateral diffusion, whereas in 3-D, not only the fluxes in x and z directions, but also the fluxes from other directions, for example j_3. The flux vector j_3 can be split into a x- ($j_{3,x}$) and a z-component ($j_{3,z}$). This extra flux contribution in x direction leads to a faster lateral growth in x–y plane.
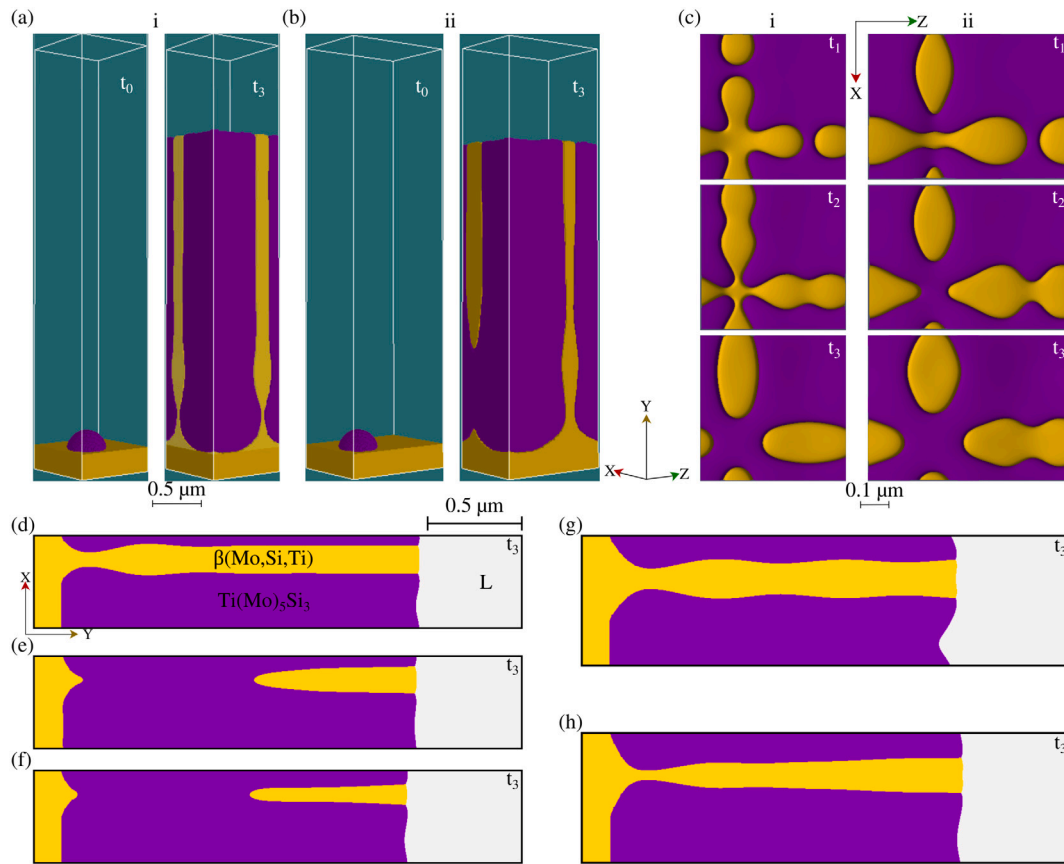
Fig. 6. (a) and (b) Side views of the morphological evolution for the cases: (i) with same lamellar spacing $\lambda_x = \lambda_z = 0.5$ μm and (ii) with different lamellar spacing $\lambda_x = 0.5$ μm and $\lambda_z = 0.7$ μm, respectively. (c) Top views of the rod eutectic growth corresponding to cases (i) and (ii). (d) and (g) 2-D simulation results of two cases: (1) The lamellar structure with a planar interface and (2) the lamellar structure with an oscillatory interface, respectively. The cross section of 3-D simulations corresponding to the cases: (e) The rod eutectic growth with $\lambda_x = \lambda_z$ in x–y plane, (f) the rod eutectic growth with $\lambda_x \neq \lambda_z$ in x–y plane, and (h) the rod eutectic growth with $\lambda_x \neq \lambda_z$ in y–z plane.
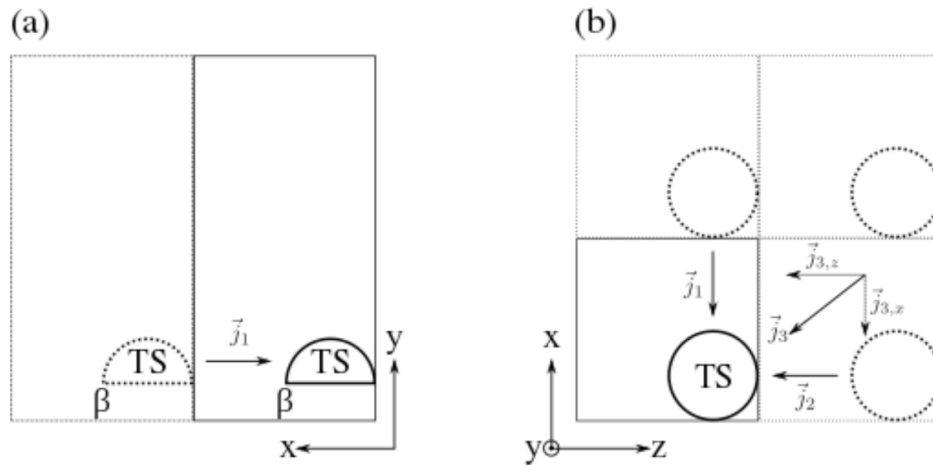

Fig. 7. Schematic illustration of the differences between 2-D and 3-D simulations.

4.3. Interfacial energy

The interfacial energy is defined as the required energy involved in creating unit area of new interface at constant temperature, volume and total number of moles [67]. In general, the interfacial energies between different phases are different and are challenging to be measured experimentally. Due to lack of precise experimental data for the interfacial energy between each two phases in Mo-Si-Ti system, we investigate how the morphological evolution of the lamellar pair is

affected by the interfacial energies in this section. The lamellar spacing is maintained as $0.5\,\mu m$, which ensures a stable lamellar structure for the considered melt compositions (see Fig. 5(c)). Fig. 8(a) and (b) depict the morphology of the solidification front of lamellae (TS and β phases) for the cases with the equilibrium contact angle $\theta = 30°$ and 150°, respectively. The lamellar pair is surrounded by the melt with the composition 26Mo-53Ti-21Si. The contact angle θ is defined as the angle between the interfacial tension vectors $\sigma_{L/\beta}$ and $\sigma_{L/TS}$, as shown in Fig. 8(b). Through changing $\sigma_{\beta/TS}$, the equilibrium value
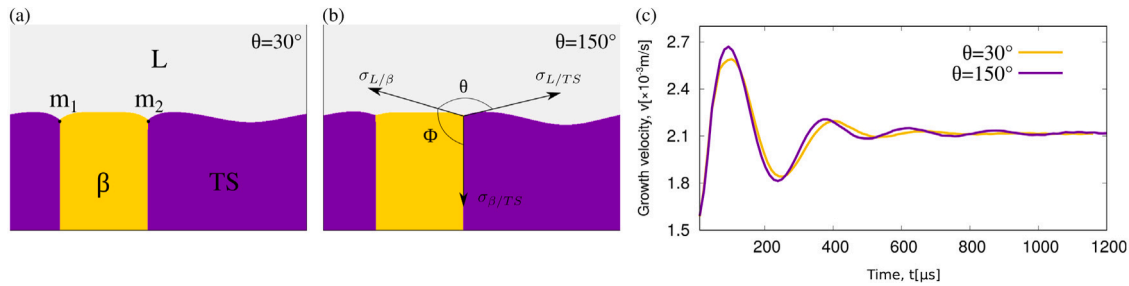
Fig. 8. (a) and (b) are the morphology of the solidification front of lamellae (TS and β phases) for the cases with the dynamic contact angle $\theta = 30°$ and 150°, respectively. (c) The temporal change of the growth velocity of β phase for the cases with different contact angle θ.

of θ is manipulated, while keeping $\sigma_{L/\beta} = \sigma_{L/TS} = 1\,\mathrm{J\,m^{-2}}$. For the two cases of $\theta = 30°$ and 150°, the solidification morphology is almost same; the growth velocity of β phase converges to the same value after the initial oscillation (Fig. 8(c)). The similar behavior in microstructure and growth velocity for the cases with different θ reveals that the interfacial energy between two solid phases has no significant influence on the morphological evolution of lamellae. When the interfacial energies between liquid and solid phases are unequal, namely $\sigma_{L/\beta} \neq \sigma_{L/TS}$, the solidification morphology is affected by the interfacial energy ratio. As an exemplary illustration in Fig. 9(a), different solidification morphologies are observed in the simulations with different equilibrium angle of Φ. The angle Φ is defined as the one between the interfacial energies $\sigma_{L/\beta}$ and $\sigma_{\beta/TS}$ (see Fig. 8(b)); the contact angle Φ is manipulated by changing $\sigma_{L/TS}$, while keeping $\sigma_{L/\beta} = \sigma_{L/TS} = 1\,\mathrm{J\,m^{-2}}$. The five representative contact angles Φ and the corresponding interfacial energies are listed in Table 5. With increasing Φ, the lamellae growth changes from curving to stable growth modes. In Fig. 9(b), a regime diagram describes the three growth modes for the five considered melt compositions. The violet, orange, and gray regions represent the curving (g_i), stable (g_{ii}), and unstable (g_{iii}) growth modes, respectively. The boundary between curving and stable growth region shifts towards the direction of increasing in Φ. The growth of solid phase is determined by two factors: one is the supersaturation in melt, which provides the driving force for the growth, and the other is the capillary force $\sigma\kappa$ against the growth (κ is the surface curvature). For the cases with same melt composition, the supersaturated melt provides the same driving force for the lamellae growth. Due to the asymmetric geometry in the two sides of β phase, the capillary force of the TS phases at two sides is unequal, giving rise to the different growth velocities at two triple points m_1 and m_2 (see Fig. 8(a)). For the case with large Φ, $\sigma_{L/TS}$ is small and therefore the difference in the capillary forces of two adjacent TS phases is small, resulting in a small difference in the growth velocity at m_1 and m_2. In this case, the unequal growth rate at m_1 and m_2 can be balanced by lateral diffusion. As a result, the lamellae exhibits a stable growth. With decreasing Φ, the interfacial energy $\sigma_{L/TS}$ increases and the difference in capillary force enhances. The effect of capillary force on the lamellae growth is pronounced, leading to a largely distinct growth rate at m_1 and m_2. Hence, the lamellae exhibits a tilt growth. In addition, an excessive growth velocity difference between two solid phases gives rise to the engulfment of one solid phase by the other one, corresponding to unstable growth of the lamellae, as shown in the gray region in Fig. 9(b). As expected, this engulfment can also be observed when a contact angle cannot be formed between these three phases. Similarly, for the cases with large supersaturation, the fast growth causes the growth rate difference to be compensated by diffusion with difficulty. Hence, the lamellae growth surrounded by high supersaturation melt is more sensitive to the difference in the interfacial energy between liquid and two solid phases.

Table 5
The contact angle Φ and corresponding interfacial energy $\sigma_{L/TS}$.

Φ (°)	30	60	90	120	150
$\sigma_{L/TS}$ (J m^{-2})	1.93	1.73	1.41	1.00	0.52

4.4. 4-Phase transformation

Based on the experimental observation in the previous study [6], the formation of the lamellar pair can also take place at the L-MS interface, that is produced by a four-phase reaction. In this section, we investigate the four-phase reaction under different supersaturations and with various lamellar spacings.

Fig. 10(a)–(d) portray the morphological evolution of the four-phase reaction for the cases with distinct supersaturations in melt. The initial melt composition in Fig. 10(a)–(d) is set to 22Mo-57Ti-21Si, 23Mo-56Ti-21Si, 26Mo-53Ti-21Si, and 28Mo-51Ti-21Si, respectively. For all four cases, the TS and β particles are initially placed on the surface of MS phase with the same radius of 0.1 μm. To better explore the four phase reaction, these two particles are separated with a distance of 0.2 μm. Due to the periodic boundary condition used at the boundaries perpendicular to the solidification front, the initial setup for the four-phase reaction is identical to that in the study of eutectic transformation in previous section. With time, TS and β phases grow towards liquid phase as well as along the L/MS interface simultaneously. For the case shown in Fig. 10(a) with the lowest supersaturation in liquid, the L/MS interface remains quasiplanar at the beginning and is bent towards the MS phase to form a "groove", when TS and β phases approach each other. This grooving indicates the melting of the MS phase during the growth of these two solid phases as both solid phases β and TS require Mo, which is provided by dissolving the MS phase via short-range diffusion in the liquid. With increasing supersaturation, this melting phenomenon weakens and the L/MS interface moves towards liquid phase to form a "ridge" for the cases illustrated in Fig. 10(c) and (d). The overall growth process of these two solid phases involves the following three parts. The first part is the direct solidification from liquid phase, namely $L \rightarrow TS$ and $L \rightarrow \beta$, that leads to the axial growth of TS and β phase. The second part consists of two peritectic transformations near the L/TS/MS and L/β/MS triple junctions that continues as long as the TS and β particles are far apart from each other. These peritectic transformations give rise to their growth along L/MS interface. The third part is the four-phase reaction, namely $L + Mo(Ti)_3Si \rightarrow Ti(Mo)_5Si_3 + \beta(Mo,Si,Ti)$, when TS and β grains have established an interface of TS-β. As a result, the MS phase melts forming a "groove" in low Mo melt compositions of cases (a) and (b). A similar melting phenomenon of parent solid phase is observed in peritectic transformation in other alloy systems, for example in Fe-C alloy [20]. For cases (c) and (d), a sufficient amount of atoms for the growth of TS
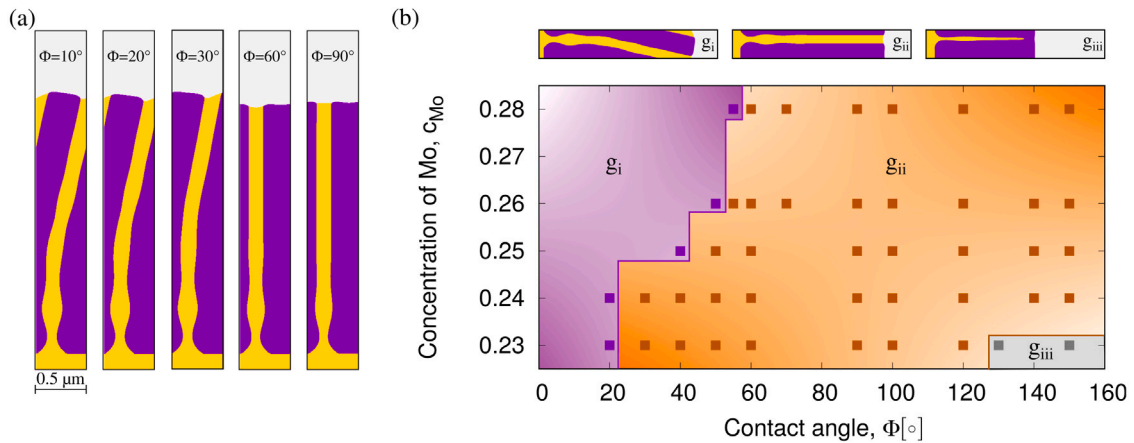
Fig. 9. (a) The solidification morphology for the cases with contact angle Φ = 10, 20, 30, 60, 90°. (b) The morphology regime diagram describing the three growth modes for five different liquid compositions: 23Mo-56Ti-21Si, 24Mo-55Ti-21Si, 25Mo-54Ti-21Si, 26Mo-53Ti-21Si, and 28Mo-51Ti-21Si and for different contact angle α.
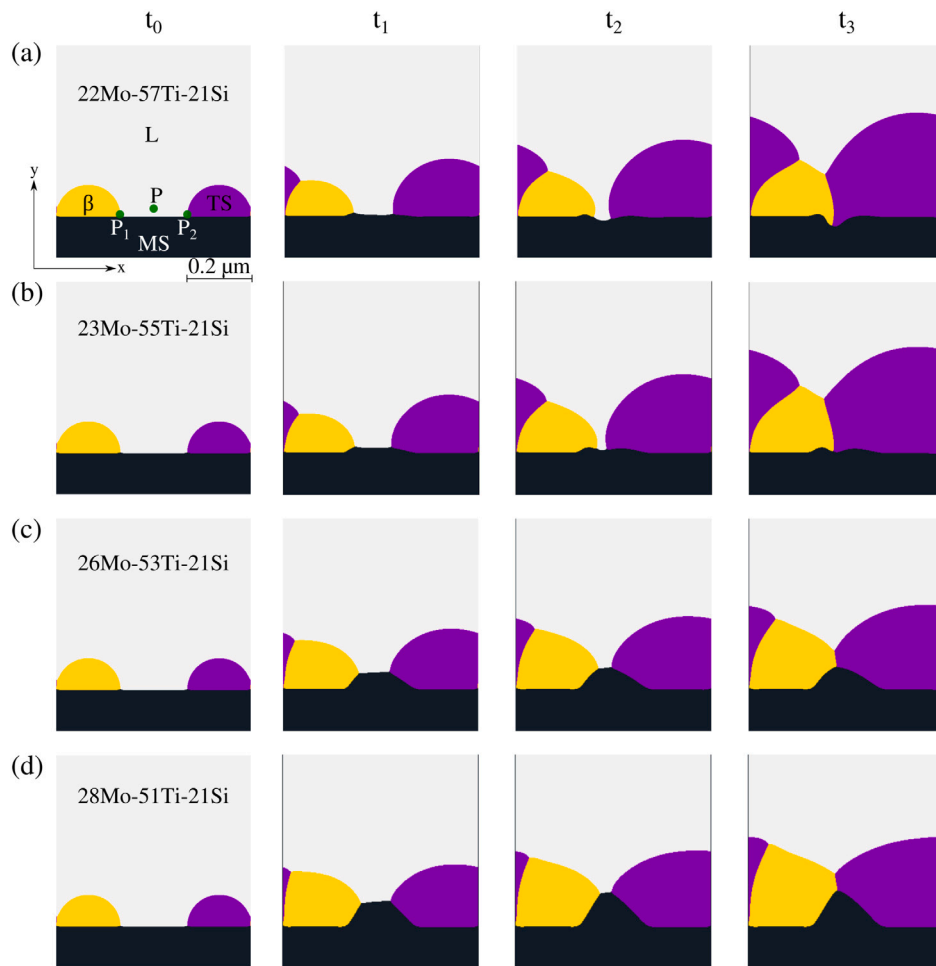

Fig. 10. (a)–(d) The morphological evolution of four-phase reaction at proceeding times t_0-t_3 for the cases with liquid concentration of 22Mo-57Ti-21Si, 23Mo-56Ti-21Si, 26Mo-53Ti-21Si, and 28Mo-51Ti-21Si, respectively.

and β phases come directly from the melt with higher supersaturation instead of consuming MS phase.

To explain the underlying mechanism for the formation of ˝groove˝ and ˝ridge˝ on the surface of the MS phase, we analyze the concentration variation of a representative spatial point p in the liquid phase under different supersaturations. The point p is defined at the position with 5 grid cells along y direction away from the midpoint of two triple junctions p_1 and p_2 to ensure that the point p is not inside the diffuse interface (see Fig. 10(a)). Fig. 11(a)–(c) depict the variation of three components (Mo, Si, and Ti) with time for the cases with melt composition 22Mo-57Ti-21Si (violet line) and 28Mo-51Ti-21Si (orange line). Since the point p disappears when the MS phase is completely covered by the TS and β phases, we consider only the concentration variation before the MS phase is engulfed. In the case
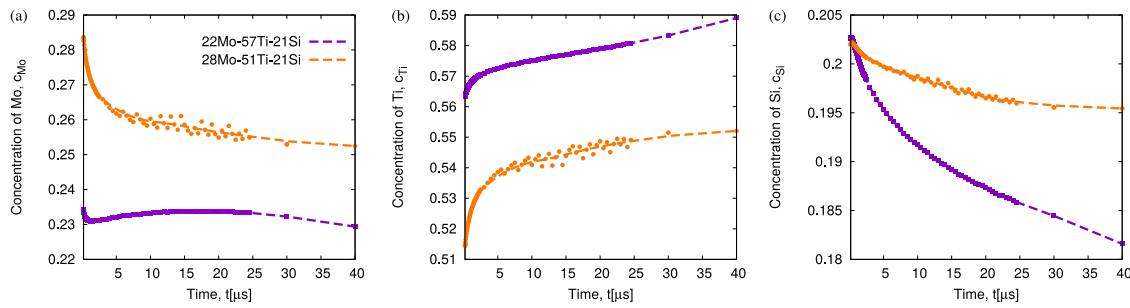
Fig. 11. (a)–(c) The variation of the concentration of Mo, Si, and Ti with time for the cases with melt composition 22Mo-57Ti-21Si and 28Mo-51Ti-21Si.

with a higher supersaturation (orange curve), the concentration of three components eventually converges to a constant value. In contrast, in the case with a lower supersaturation, the concentration of Mo increases at the beginning and decreases after a certain time, the concentration of Si reduces and the concentration of Ti enriches. As the sum of the three concentrations is unity, this system is characterized by two independent components Mo and Si. A comparison between these two cases demonstrates that a higher supersaturation leads to a larger concentration of Mo and Si that provides the driving force for phase transformation $L \rightarrow MS$, while the phase transformation $MS \rightarrow L$ occurs in the other case, where the concentrations of Mo and Si are lower. As a consequence, L/MS interface shifts towards liquid phase in the case with a higher supersaturation, whereas L/MS interface moves towards MS phase in the case with a lower supersaturation.

When the TS and β phases cover the MS phase completely, the four-phase reaction is inhibited and subsequently eutectic transformation takes place. In the following, we investigate the influence of the preceding four-phase reaction on the morphological evolution of the eutectic lamellae.

The initial setup for the simulations with melt composition 24Mo-55Ti-21Si and 26Mo-53Ti-21Si is illustrated in Fig. 12(a) and (f), respectively. Two semicircular particles TS and β with the same radius of 0.1 μm are placed tangentially to each other on the L/MS interface. Due to the periodic boundary condition used at the boundaries perpendicular to the solidification front, the selected volume is identical to that in the previous discussion of four-phase reaction in this section. By adjusting the lamellar spacing, we control the contact between liquid and MS phase and thus manipulate the four-phase reaction. Fig. 12(b)–(e) show the microstructure of the eutectic lamellae for the cases with λ = 0.4, 0.5, 0.6, and 0.7 μm at the time t= 1540 μs, respectively. For all the four cases, the lamellar structure forms on the MS surface. In the case (b), the MS phase is completely covered by the two solid phases at the beginning, which prevents the four-phase reaction. In this case, the formation of lamellar structure is only caused by eutectic transformation. For the cases involving with four phase reaction (Fig. 12(c)–(e)), the eutectic lamellae grows with an orientation angle deviating from y-direction. In contrast, the lamellar structure formed only by eutectic transformation in the case (b) grows along y-direction without orientation angle. In the same manner, we investigate the morphology of the lamellar pair with melt composition 26Mo-53Ti-21Si at the time t= 1860 μs, as illustrated in Fig. 12(g) to (j). In case (g) only with eutectic transformation, the lamellar pair exhibits a straight growth after reaching a steady state, while in other three cases, an oblique growth of the eutectic lamellae caused by the active four-phase reaction is observed. In order to characterize the tilted growth of the lamellar pair, we measure the angle between the TS/β interface and y-direction, when the growth reaches a steady state (see Fig. 12(i)). For the cases with an oscillatory TS/β interface, we connect all peaks and all valleys of the interface by two lines, and calculate the orientation angle by using the average tangent of these two lines. The orientation angles for the cases (b) to (e) and (g) to (j) are listed

Table 6
The orientation angle of the lamellae for the cases with melt composition 24Mo-55Ti-21Si and 26Mo-53Ti-21Si.

λ (μm) Cases	0.4	0.5	0.6	0.7
24Mo-55Ti-21Si	0°	0.9°	2.2°	3.7°
26Mo-53Ti-21Si	0°	1.3°	4.4°	9.5°

in Table 6. For the cases under same supersaturation, the orientation angle of the lamellar growth increases with λ.

As discussed in Section 2, the deviation of the interfacial concentration from the equilibrium concentration leads to a difference in the grand chemical potential, which provides the driving force for the phase transition. Therefore, we explain the reasons for the tilted growth by analyzing the concentration distribution ahead of the solidification front. Fig. 13(a) shows the concentration profile of the three components along the black dashed line (see Fig. 12(b)) for the four cases with λ = 0.4, 0.5, 0.6, and 0.7 μm. As an exemplary explanation, we choose the concentration profile of the cases with melt composition 24Mo-55Ti-21Si at the time t= 1540 μs. For all three components, their concentration distributions along the black dashed line become more asymmetrical with respect to the growth direction and the difference between maximum and minimum concentration becomes larger, when λ increases. The asymmetrical composition profile is caused by the asynchronous movements of triple points L/TS/β on both side of TS phase, which in turn is affected by the liquid concentration ahead of them. Hence, we use the temporal concentration variation of p_1 and p_2 after occurrence of eutectic transformation, as shown in Fig. 13(b), to characterize the motions of two triple points. The points p_1 and p_2 are defined at the position in liquid phase, which are 5 grid cells away in the y-direction from the triple point L/TS/β on either side of the TS phase (see Fig. 12(e)). The violet and orange lines in Fig. 13(b) represent the concentration of point p_1 and p_2 varying with time, respectively. For both points, the concentrations of Mo and Si decrease at the beginning and then increase with time, while the Ti concentration increases initially and decreases after a certain time. A comparison between the concentration variation of the two points shows that the Ti concentration at two points maintain identical, the concentration of Mo increases faster at p_2 than p_1, whereas the opposite tendency is observed for Si concentration with time. According to the previous discussion, two different peritectic transitions occurs at the L/TS/MS and L/β/MS triple points at the beginning. When the MS phase is completely covered by TS and β grains, L/TS/MS and L/β/MS triple points disappear and two new L/TS/β triple points appear indicating the beginning of the eutectic transformation. Under the influence of two different peritectic transitions, the concentrations in front of these triple points are not the same. This difference gives rise to the different movement velocity of triple points. As a result, the lamellar pair grows with an orientation angle. Exemplarily, we study the morphological evolution of the lamellar pair during the four-phase reaction with the melt composition 26Mo-53Ti-21Si in 3-D, as shown in Fig. 14. For a
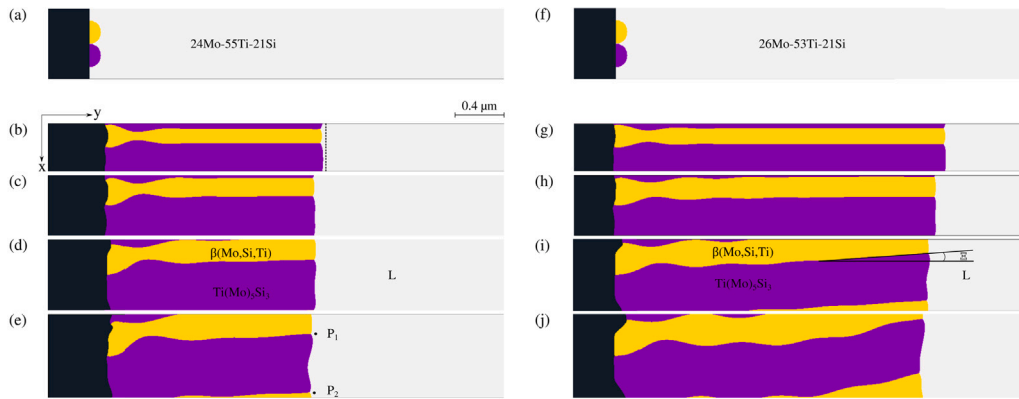
Fig. 12. (a) and (f): The initial setup for the simulations with melt composition 24Mo-55Ti-21Si and 26Mo-53Ti-21Si. (b)–(e): The microstructure of eutectic lamellae with melt composition 24Mo-55Ti-21Si for the cases with $\lambda = 0.4$, 0.5, 0.6, and 0.7 μm at the time t= 1540 μs, respectively. (g)–(j): The microstructure of eutectic lamellae with melt composition 26Mo-53Ti-21Si for the cases with $\lambda = 0.4$, 0.5, 0.6, and 0.7 μm at the time t= 1860 μs, respectively.
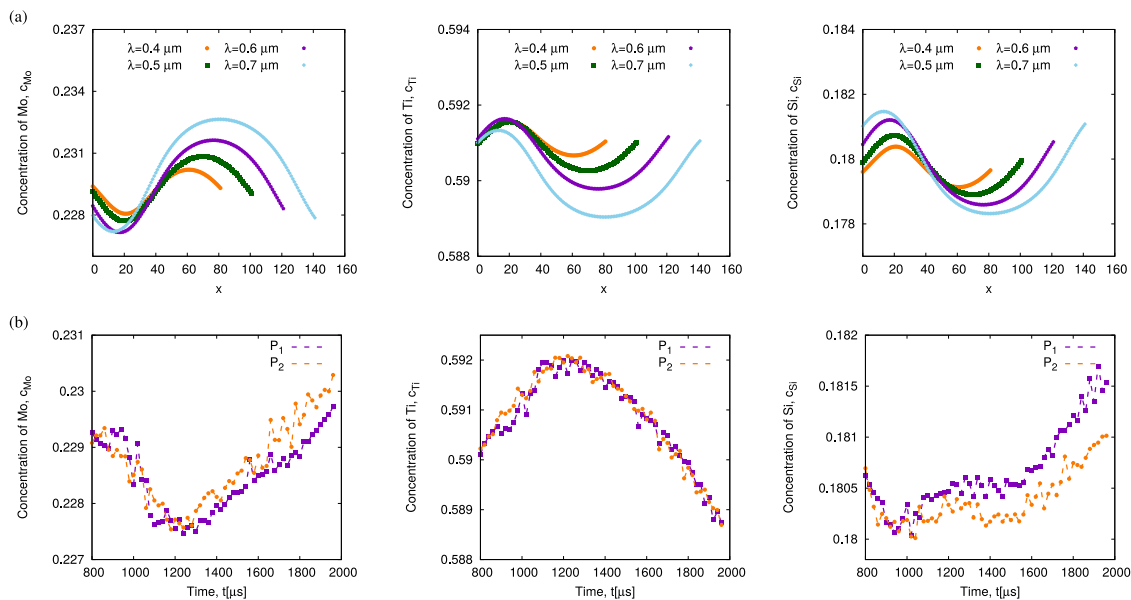

Fig. 13. (a) The concentration profile of three components along the black dashed line in Fig. 12(b), for the four cases with $\lambda = 0.4$, 0.5, 0.6, and 0.7 μm. (b) The temporal concentration variation of p_1 and p_2.

better observation, Fig. 14(b)–(d) portray the cross section of the 3-D simulation. In Fig. 14, the tilted growth of the lamellar pair is also observed in 3-D. Compared with the 2-D simulation, the morphology of the lamellar pair is more complex due to the additional contribution in the third dimension. The detailed discussion and systematic analysis of the lamellar growth morphologies in 3-D will be addressed in a forthcoming work.

5. Conclusion

By using the phase-field method, we have systematically studied the lamellae growth caused by a eutectic transformation as well as by a four-phase reaction in Mo-Si-Ti alloy through 2-D and 3-D simulations, with inputs from the CALPHAD database.

For the eutectic transformation, the 2-D simulation results show that the microstructural evolution of lamellar pair is affected by the supersaturation and the lamellar spacing, which is consistent with Jackson–Hunt theory. The lamellae growth exhibits a transformation from unstable to metastable through stable growth mode with increasing lamellar spacing. Through the simulations with different supersaturation and with various lamellar spacing, we obtain a microstructure

selection map for distinct growth morphologies. In 3-D simulation, the eutectic growth of the rods under the influence of neighbor particles in the third dimension displays a distinct microstructure compared to 2-D simulation. In addition, the stable growth of lamellae in 3-D is restricted in a region with smaller lamellar spacing than in 2-D. The reason for the difference between 2-D and 3-D is that an additional diffusion flux in 3-D leads to faster growth in the plane perpendicular to the solidification direction. When the TS phases are set asymmetrically at the two sides of β phase, the solidification morphology of the lamellar pair under different supersaturations in melt or with distinct solid–liquid interfacial energies shows three different types: curving, stable, and unstable growth modes. The final morphology is determined by the combining effect of diffusion, reaction as well as the capillary force.

In the four-phase reaction, we observe the formation of "groove" and "ridge" of Mo(Ti)$_3$Si phase in the melt with lower and higher supersaturation, respectively. These phenomena indicate that the remelting of this phase at lower supersaturation provides the solute for the lamellae growth, while the melt with higher supersaturation directly offers a sufficient amount of atoms for its growth. Furthermore, the lamellar pair on the surface of Mo(Ti)$_3$Si grain grows with a certain
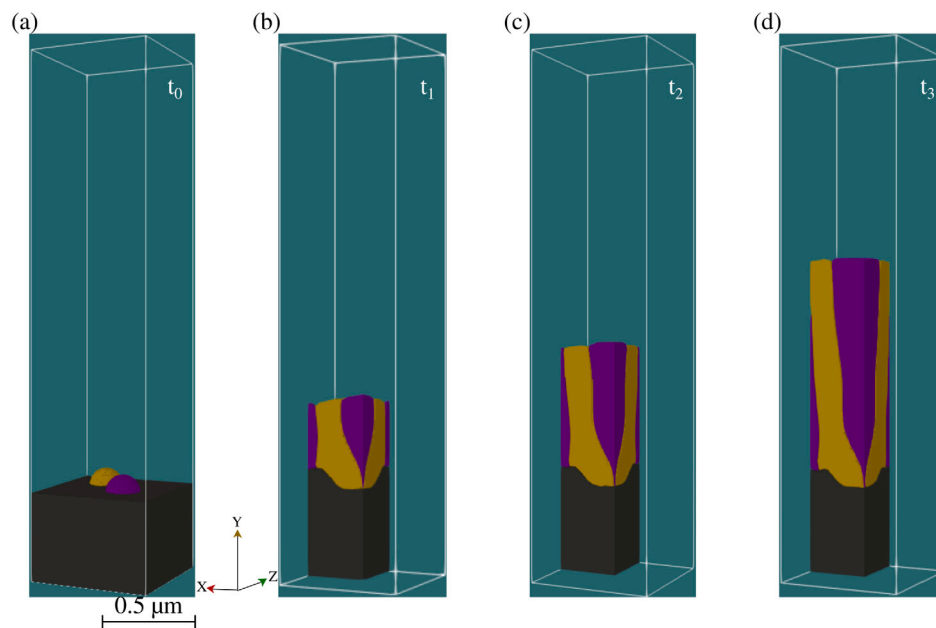
Fig. 14. Side view of the morphological evolution for the four-phase reaction.

orientation angle during the four-phase reaction and the orientation angle increases with the enlarging lamellar spacing. The tilted growth is caused by two different peritectic transitions and the associated asymmetric concentration profiles in the vicinity of two triple junctions, namely $L/Ti(Mo)_5Si_3/Mo(Ti)_3Si$ and $L/\beta(Mo,Si,Ti)/Mo(Ti)_3Si$.

By simulating the lamellae growth during a eutectic transformation in Mo-Si-Ti alloy, we have constructed a microstructure selection map, which should be helpful to the experimental studies and the industrial applications in the development of new tailored materials by new designing the microstructural morphology. Our computational investigation on the four-phase reaction provides additional insight into the underlying growth mechanism for the formation of the lamellae pair in Mo-Si-Ti alloy. The study on the bending growth of lamellae explains two possible reasons for this phenomenon found in experiments.

Declaration of competing interest

The authors declare that they have no known competing financial interests or personal relationships that could have appeared to influence the work reported in this paper.

Acknowledgments

Appendix A. Supplementary data

Supplementary material related to this article can be found online at https://doi.org/10.1016/j.actamat.2023.119178.

References

[1] J.A. Lemberg, R.O. Ritchie, Mo-Si-B alloys for ultrahigh-temperature structural applications, Adv. Mater. 24 (26) (2012) 3445–3480.

[2] J.H. Perepezko, The hotter the engine, the better, Science 326 (5956) (2009) 1068–1069.

[3] M.A. Azim, D. Schliephake, C. Hochmuth, B. Gorr, H.-J. Christ, U. Glatzel, M. Heilmaier, Creep resistance and oxidation behavior of novel Mo-Si-B-Ti alloys, JOM 67 (11) (2015) 2621–2628.

[4] D. Schliephake, A. Kauffmann, X. Cong, C. Gombola, M. Azim, B. Gorr, H.-J. Christ, M. Heilmaier, Constitution, oxidation and creep of eutectic and eutectoid Mo-Si-Ti alloys, Intermetallics 104 (2019) 133–142.

[5] S. Obert, A. Kauffmann, M. Heilmaier, Characterisation of the oxidation and creep behaviour of novel Mo-Si-Ti alloys, Acta Mater. 184 (2020) 132–142.

[6] Y. Yang, Y. Chang, L. Tan, Y. Du, Experimental investigation and thermodynamic descriptions of the Mo–Si–Ti system, Mater. Sci. Eng. A 361 (1–2) (2003) 281–293.

[7] J.Y. Huh, K. Hong, Y. Kim, K. Kim, Phase field simulations of intermetallic compound growth during soldering reactions, J. Electron. Mater. 33 (10) (2004) 1161–1170.

[8] M.S. Park, S.L. Gibbons, R. Arróyave, Phase-field simulations of intermetallic compound evolution in Cu/Sn solder joints under electromigration, Acta Mater. 61 (19) (2013) 7142–7154.

[9] F. Wang, B. Nestler, A phase-field study on the formation of the intermetallic Al2Au phase in the Al–Au system, Acta Mater. 95 (2015) 65–73.

[10] D.-C. Kim, T. Ogura, R. Hamada, S. Yamashita, K. Saida, Establishment of a theoretical model based on the phase-field method for predicting the γ phase precipitation in Fe–Cr–Ni ternary alloys, Mater. Today Commun. 26 (2021) 101932.

[11] M. Berghoff, B. Nestler, Phase field crystal modeling of ternary solidification microstructures, Comput. Condens. Matter 4 (2015) 46–58.

[12] S. Gyoon Kim, W. Tae Kim, T. Suzuki, M. Ode, Phase-field modeling of eutectic solidification, J. Cryst. Growth 261 (1) (2004) 135–158.

[13] M. Apel, B. Boettger, H.-J. Diepers, I. Steinbach, 2D and 3D phase-field simulations of lamella and fibrous eutectic growth, J. Cryst. Growth 237–239 (2002) 154–158, The thirteenth international conference on Crystal Growth in conjunction with the eleventh international conference on Vapor Growth and Epitaxy.

[14] F. Drolet, K.R. Elder, M. Grant, J.M. Kosterlitz, Phase-field modeling of eutectic growth, Phys. Rev. E 61 (2000) 6705–6720.

[15] A. Karma, A. Sarkissian, Morphological instabilities of lamellar eutectics, Metall. Mater. Trans. A 27 (3) (1996) 635–656.

[16] D. Phelan, M. Reid, R. Dippenaar, Kinetics of the peritectic phase transformation: In-situ measurements and phase field modeling, Metall. Mater. Trans. A 37 (3) (2006) 985–994.

[17] J. Tiaden, Phase field simulations of the peritectic solidification of Fe–C, J. Cryst. Growth 198–199 (1999) 1275–1280.

[18] S. Pan, M. Zhu, M. Rettenmayr, A phase-field study on the peritectic phase transition in Fe-C alloys, Acta Mater. 132 (2017) 565–575.

[19] M. Ohno, K. Matsuura, Diffusion-controlled peritectic reaction process in carbon steel analyzed by quantitative phase-field simulation, Acta Mater. 58 (18) (2010) 6134–6141.

[20] Y. Cai, F. Wang, Z. Zhang, B. Nestler, Phase-field investigation on the peritectic transition in Fe-C system, Acta Mater. 219 (2021) 117223.

[21] A. Karma, Phase-field model of eutectic growth, Phys. Rev. E 49 (1994) 2245–2250.

[22] A.A. Wheeler, G. McFadden, W. Boettinger, Phase-field model for solidification of a eutectic alloy, Proc. R. Soc. Lond. Ser. A Math. Phys. Eng. Sci. 452 (1946) (1996) 495–525.

[23] J. Tiaden, B. Nestler, H.J. Diepers, I. Steinbach, The multiphase-field model with an integrated concept for modelling solute diffusion, Physica D 115 (1) (1998) 73–86.

[24] I. Steinbach, F. Pezzolla, B. Nestler, M. Seeß elberg, R. Prieler, G.J. Schmitz, J.L.L. Rezende, A phase field concept for multiphase systems, Physica D 94 (3) (1996) 135–147.

[25] J. Eiken, B. Böttger, I. Steinbach, Multiphase-field approach for multicomponent alloys with extrapolation scheme for numerical application, Phys. Rev. E 73 (2006) 066122.

[26] B. Nestler, A.A. Wheeler, A multi-phase-field model of eutectic and peritectic alloys: Numerical simulation of growth structures, Physica D 138 (1) (2000) 114–133.

[27] A. Choudhury, B. Nestler, Grand-potential formulation for multicomponent phase transformations combined with thin-interface asymptotics of the double-obstacle potential, Phys. Rev. E 85 (2012) 021602.

[28] P. Steinmetz, M. Kellner, J. Hötzer, B. Nestler, Quantitative comparison of ternary eutectic phase-field simulations with analytical 3D Jackson–Hunt approaches, Metall. Mater. Trans. B 49 (1) (2018) 213–224.

[29] M. Kellner, J. Hötzer, E. Schoof, B. Nestler, Phase-field study of eutectic colony formation in NiAl-34Cr, Acta Mater. 182 (2020) 267–277.

[30] Z. Tu, J. Zhou, L. Tong, Z. Guo, A phase-field study of lamellar eutectic growth with solid-solid boundary anisotropy, J. Cryst. Growth 532 (2020) 125439.

[31] V.V. Podolinsky, Y. Taran, V.G. Drykin, Eutectic solidification in organic systems, J. Cryst. Growth 74 (1) (1986) 57–66.

[32] K. Dargahi Noubary, M. Kellner, B. Nestler, Rotating directional solidification of ternary eutectic microstructures in Bi-In-Sn: A phase-field study, Materials 15 (3) (2022).

[33] B. Nestler, H. Garcke, B. Stinner, Multicomponent alloy solidification: Phase-field modeling and simulations, Phys. Rev. E 71 (2005) 041609.

[34] O. Kazemi, G. Hasemann, M. Krüger, T. Halle, Phase field simulation of a directional solidification of a ternary eutectic Mo-Si-B alloy, IOP Conf. Ser.: Mater. Sci. Eng. 118 (1) (2016) 012028.

[35] M. Rahul, S. Samal, G. Phanikumar, Metastable microstructures in the solidification of undercooled high entropy alloys, J. Alloys Compd. 821 (2020) 153488.

[36] J. Park, J.-H. Kang, C.-S. Oh, Phase-field simulations and microstructural analysis of epitaxial growth during rapid solidification of additively manufactured AlSi10Mg alloy, Mater. Des. 195 (2020) 108985.

[37] M. Apel, B. Böttger, J. Rudnizki, P. Schaffnit, I. Steinbach, Grain growth simulations including particle pinning using the multiphase-field concept, ISIJ Int. 49 (7) (2009) 1024–1029.

[38] J. Eiken, Discussion of the accuracy of the multi-phase-field approach to simulate grain growth with anisotropic grain boundary properties, ISIJ Int. 60 (8) (2020) 1832–1834.

[39] J. Kundin, E. Pogorelov, H. Emmerich, Phase-field modeling of the microstructure evolution and heterogeneous nucleation in solidifying ternary Al–Cu–Ni alloys, Acta Mater. 83 (2015) 448–459.

[40] A. Choudhury, B. Nestler, Grand-potential formulation for multicomponent phase transformations combined with thin-interface asymptotics of the double-obstacle potential, Phys. Rev. E 85 (2) (2012) 021602.

[41] R.W. Balluffi, S.M. Allen, W.C. Carter, Kinetics of Materials, John Wiley & Sons, 2005.

[42] P.-R. Cha, D.-H. Yeon, J.-K. Yoon, Phase-field model for multicomponent alloy solidification, J. Cryst. Growth 274 (1) (2005) 281–293.

[43] B. Echebarria, R. Folch, A. Karma, M. Plapp, Quantitative phase-field model of alloy solidification, Phys. Rev. E 70 (6) (2004) 061604.

[44] P. Shewmon, Diffusion in Solids, Springer, 2016.

[45] R.C. Jones, W.H. Furry, The separation of isotopes by thermal diffusion, Rev. Modern Phys. 18 (1946) 151–224.

[46] M. Fierz, S. Weimer, H. Burtscher, Design and performance of an optimized electrical diffusion battery, J. Aerosol Sci. 40 (2) (2009) 152–163.

[47] J. Hoekstra, A.P. Sutton, T.N. Todorov, A.P. Horsfield, Electromigration of vacancies in copper, Phys. Rev. B 62 (2000) 8568–8571.

[48] F. Larché, P.W. Voorhees, Diffusion and stresses: Basic thermodynamics, in: Defect and Diffusion Forum, vol. 129, Trans Tech Publ, 1996, pp. 31–36.

[49] Q.-L. Cao, D.-H. Huang, J.-S. Yang, M.-J. Wan, F.-H. Wang, Transport properties and the entropy-scaling law for liquid tantalum and molybdenum under high pressure, Chin. Phys. Lett. 31 (6) (2014) 66202.

[50] A. Meyer, J. Horbach, O. Heinen, D. Holland-Moritz, T. Unruh, Self diffusion in liquid titanium: Quasielastic neutron scattering and molecular dynamics simulation, in: Diffusion in Materials - DIMAT2008, in: Defect and Diffusion Forum, vol. 289, Trans Tech Publications Ltd, 2009, pp. 609–614.

[51] Y. Liu, W.-f. Wei, K.-c. Zhou, L.-f. Chen, H.-p. Tang, Microstructures and mechanical behavior of PM Ti-Mo alloy, J. Central South Univ. Technol. 10 (2) (2003) 81–86.

[52] C. Fu, M. Yoo, Interfacial energies in two-phase TiAl-Ti3Al alloy, Scr. Mater. 37 (10) (1997) 1453–1459.

[53] G. Kaptay, Modelling interfacial energies in metallic systems, in: Materials Science Forum, vol. 473, Trans Tech Publ, 2005, pp. 1–10.

[54] Y. Yang, Y. Chang, L. Tan, W. Cao, Multiphase equilibria in the metal-rich region of the Mo–Ti–Si–B system: Thermodynamic prediction and experimental validation, Acta Mater. 53 (6) (2005) 1711–1720.

[55] R.D. Ramdan, T. Takaki, Y. Tomita, Free energy problem for the simulations of the growth of Fe_2B phase using phase-field method, Mater. Trans. 49 (11) (2008) 2625–2631.

[56] H.-S. Kim, H.-J. Lee, Y.-S. Yu, Y.-S. Won, Three-dimensional simulation of intermetallic compound layer growth in a binary alloy system, Acta Mater. 57 (4) (2009) 1254–1262.

[57] Y. Cai, F. Wang, M. Selzer, B. Nestler, Phase-field investigation on the growth orientation angle of aluminum carbide with a needle-like structure at the surface of graphite particles, Modelling Simul. Mater. Sci. Eng. 27 (6) (2019) 065010.

[58] O. Redlich, A. Kister, Algebraic representation of thermodynamic properties and the classification of solutions, Ind. Eng. Chem. 40 (2) (1948) 345–348.

[59] K. Dargahi Noubary, M. Kellner, J. Hötzer, M. Seiz, H.J. Seifert, B. Nestler, Data workflow to incorporate thermodynamic energies from Calphad databases into grand-potential-based phase-field models, J. Mater. Sci. 56 (20) (2021) 11932–11952.

[60] S. Obert, A. Kauffmann, S. Seils, S. Schellert, M. Weber, B. Gorr, H.-J. Christ, M. Heilmaier, On the chemical and microstructural requirements for the pesting-resistance of Mo–Si–Ti alloys, J. Mater. Res. Technol. 9 (4) (2020) 8556–8567.

[61] S. Majumdar, P.K. Singh, A.K. Pandey, G.N. Rao, Kinetics of oxide scale growth on a (Ti, Mo)$_5$Si$_3$ based oxidation resistant Mo-Ti-Si alloy at 900-1300°c, High Temp. Mater. Processes 38 (2019) (2019) 533–540.

[62] A. Vondrous, M. Selzer, J. Hötzer, B. Nestler, Parallel computing for phase-field models, Int. J. High Perf. Comput. Appl. 28 (1) (2014) 61–72.

[63] M. Ginibre, S. Akamatsu, G. Faivre, Experimental determination of the stability diagram of a lamellar eutectic growth front, Phys. Rev. E 56 (1997) 780–796.

[64] K. Alain, S. Armand, Morphological instabilities of lamellar eutectics, Metall. Mater. Trans. A 27 (3) (1996) 635–656.

[65] M. Perrut, S. Bottin-Rousseau, G. Faivre, S. Akamatsu, Dynamic instabilities of rod-like eutectic growth patterns: A real-time study, Acta Mater. 61 (18) (2013) 6802–6808.

[66] K.A. Jackson, J.D. Hunt, Lamellar and rod eutectic growth, in: P. Pelcé (Ed.), Dynamics of Curved Fronts, Academic Press, San Diego, 1988, pp. 363–376.

[67] G.H. Meier, Introduction to surface quantities, in: Thermodynamics of Surfaces and Interfaces: Concepts in Inorganic Materials, Cambridge University Press, 2014, pp. 40–72.